

# Periodic-orbit approach to the nuclear shell structures with power-law potential models I: – Bridge orbits and prolate-oblate asymmetry –

Ken-ichiro Arita

*Department of Physics, Nagoya Institute of Technology, Nagoya 466-8555, Japan*

(Dated: May 31, 2012)

Deformed shell structures in nuclear mean-field potentials are systematically investigated as functions of deformation and surface diffuseness. As the mean field model to investigate nuclear shell structures in wide range of mass numbers, we propose the radial power-law potential model,  $V \propto r^\alpha$ , which enables us a simple semiclassical analysis by the use of its scaling property. We find remarkable shell structures emerge at certain combinations of deformation and diffuseness parameters, and they are closely related to the periodic orbit bifurcations. In particular, significant roles of the “bridge orbit bifurcations” for normal and superdeformed shell structures are pointed out. It is shown that the prolate-oblate asymmetry in deformed shell structures is clearly understood from the contribution of bridge orbit to the semiclassical level density. The roles of bridge orbit bifurcations to the emergence of superdeformed shell structures are also discussed.

PACS numbers: 21.10.Gv, 03.65.Sq, 05.45.-a

## I. INTRODUCTION

Shell structures in single-particle energy spectra play essential roles in nuclear ground-state deformations and their stabilities. Using the semiclassical trace formula, single-particle level density is expressed as the sum over contribution of classical periodic orbits in the corresponding classical Hamiltonian[1, 2]. The quantum fluctuations in many-body properties such as energy and deformations are related with gross shell structure in single-particle spectra determined by some of the shortest periodic orbits. Therefore, one can analyze many-body quantum dynamics in terms of the properties of a few important classical periodic orbits. The single-particle shell structures are sensitively changed by varying potential parameters such as deformations, and we have found that bifurcations of short periodic orbits play significant roles in emergence of remarkable shell effects. It is a quite interesting phenomena that the regularity of quantum spectra is enhanced by the periodic orbit bifurcation which is the precursor of chaos in classical dynamics. In this paper, we would like to show that the above semiclassical mechanism for the enhancement of quantum shell effect would elucidate several problems in nuclear structure physics.

As phenomenological mean-field potentials, modified oscillator (MO) and Woods-Saxon (WS) models are successfully employed in shell correction approaches. For simpler and qualitative descriptions of the properties of shell structures, harmonic oscillator (HO) and infinite-well (cavity) potentials are frequently aided for light and heavy systems, respectively. Axially-symmetric anisotropic HO potential model successfully explain the magic numbers of light nuclei, emergence of superdeformed shell structures, and so on. For heavier nuclei, radial profile of the potential around the nuclear surface becomes more sharp and it looks more similar to a square well potential. In order to prevent from complexity of treating continuum states, WS potential is sometimes approximated by infinite well potential (cavity). The cavity system, as well as HO system, is integrable under spheroidal deformation due to the existence of a non-trivial dynamical symmetry, and several classical and quantum mechanical quan-

ties are obtained analytically. It also accepts several useful techniques to calculate quantum eigenvalue spectra, since the Schrödinger equation is equivalent to the Laplace equation with Dirichlet boundary condition.

The HO and cavity systems have significant difference in deformed shell structures. In axially-deformed HO system, the ways which degeneracy of levels are resolved due to deformation are nearly symmetric (under rotation about the degenerate spherical point by angle  $\pi$ ) in prolate and oblate sides, while those in cavity system are apparently asymmetric (in the sense same as above). Such asymmetry has been considered as the origin of so called *prolate-shape dominance* in nuclear ground-state deformations; a well-known experimental fact that the most of the ground-states of medium-mass to heavy nuclei have prolate shapes rather than oblate shapes. Its origin has been discussed since the discovery of the nuclear ground state deformation[3–6]. This predominance has been reproduced theoretically in microscopic calculations. In Hartree-Fock+BCS calculations with Skyrme interaction[4], most of the deformed ground state solutions are found to have prolate shapes. In order to pin down the essential parameter which causes prolate-shape dominance, systematic Nilsson-Strutinsky calculations throughout the nuclear chart have been made[5], and the distribution of ground-state deformations are examined by varying the strengths of  $l^2$  and  $ls$  terms in Nilsson Hamiltonian. They found that the prolate-shape dominance is realized under strong correlation between  $l^2$  and  $ls$  terms. The recent analysis by Takahara et al. based on Woods-Saxon-Strutinsky calculations also supports those results[6]. Hamamoto and Mottelson compared the oblate and prolate deformation energy from the summation of single-particle energies with spheroidal HO and cavity models, and have shown that the prolate-shape dominance is only found in cavity model. They considered the origin of that prolate-shape dominance as the asymmetric way of level fannings in prolate and oblate sides for a potential with sharp surface, and have shown that the above asymmetry is explained from the different roles of interaction between single-particle levels in prolate and oblate sides[7].

We expect that the semiclassical periodic-orbit theory (POT) holds the key for deeper understandings of above shell

structures responsible for prolate-shape dominance. In POT, semiclassical level density is expressed as

$$g(E) = \bar{g}(E) + \sum_{\beta} A_{\beta}(E) \cos\left(\frac{S_{\beta}(E)}{\hbar} - \frac{\pi\mu_{\beta}}{2}\right). \quad (1.1)$$

$\bar{g}$  is the average level density which is given as the contribution of zero-length orbit, and the second term on the right-hand side gives the fluctuations around  $\bar{g}$ . The sum is taken over all the classical periodic orbits  $\beta$  which exist for given energy  $E$ .  $S_{\beta} = \oint_{\beta} \mathbf{p} \cdot d\mathbf{r}$  is the action integral, and  $\mu_{\beta}$  is the geometric phase index determined by the number of conjugate points along the orbit. In general, each periodic orbit (PO)  $\beta$  changes its size and shape with increasing energy  $E$ , and the action integral  $S_{\beta}$  is a monotonically increasing function of  $E$ . Thus, each cosine term in the PO sum (1.1) is a regularly oscillating function of energy whose period of oscillation  $\delta E$  is given through the relation

$$\delta S_{\beta} \sim \frac{\partial S_{\beta}}{\partial E} \delta E \sim 2\pi\hbar, \quad \delta E \sim \frac{2\pi\hbar}{T_{\beta}}, \quad (1.2)$$

where  $T_{\beta} = \partial S_{\beta} / \partial E$  is time period of the orbit  $\beta$ . Therefore, a gross shell structure (large  $\delta E$ ) is associated with short periodic orbits (small  $T_{\beta}$ ).

The relation between coarse-grained quantum level density oscillations and classical periodic orbits in spherical cavity model was first discussed by Balian and Bloch[2]. They show that the modulations in quantum level density oscillations are clearly understood as the interference effect of periodic orbits with different lengths. This idea has been successfully applied to the problem of supershell structure in metallic clusters[8]. Strutinsky et al.[9] applied periodic orbit theory (POT)[1, 2] to the cavity model with spheroidal deformation and discussed the properties of deformed shell structures in medium-mass to heavy nuclei in terms of classical periodic orbits[9]. Frisk made more extensive POT calculations to reproduce quantum level density by the semiclassical formula[10]. He also suggested the relation between classical periodic orbits and prolate-oblate asymmetry in deformed shell structures, which might be responsible for prolate-shape dominance discussed above. Those works have proved virtue of semiclassical POT for clear understandings of the properties of finite quantum systems.

It should be emphasized here that unique deformed shell structures are developed when the contributions of certain periodic orbits are considerably enhanced. The magnitude of shell effect is related with the amplitude factor  $A_{\beta}$  in Eq. (1.1). This amplitude factor has important dependency on the stability of the orbit, which is generally very sensitive to the potential parameters such as deformations. In particular, stability factor sometimes exhibit significant enhancement at periodic orbit bifurcation, where new periodic orbits emerge from an existing periodic orbit. Near the bifurcation point, classical orbits surrounding the stable periodic orbit form a quasi-periodic family, which make coherent contribution to the level density. This is an important mechanism for the growth of deformed shell structures.

A typical example is so-called superdeformed shell structure. It is known that single-particle spectra exhibit remarkable shell effect at very large quadrupole-type deformation

with axis ratio around 2:1. In anisotropic HO model, this shell structure is related with the periodic orbit condition; all the classical orbits become periodic at  $\omega_{\perp} = 2\omega_z$  and they make very large contribution to the level density fluctuation. In the cavity model, one also finds significant shell effect around 2:1 deformation, and it is related with the bifurcations of equatorial periodic orbits through which three-dimensional (3D) periodic orbits emerge[11, 12]. It should be interesting to explore the intermediate situation between the above two limits, which might correspond to the actual nuclear situation.

Our purpose in this paper is to understand the transition of deformed shell structure from light to heavy nuclei in terms of classical periodic orbits. It requires a mean-field like WS potential model. Semiclassical quantization in spherical and deformed WS-like potentials have been examined in Refs. [13, 14], but the relation between classical periodic orbits with quantum level densities have not been discussed. As we show, WS potential inside the nuclear radius  $R_A$  is nicely approximated by power-law potential which has simpler radial dependence  $V \propto r^{\alpha}$ . This approximation simplify both quantum and classical calculations and one has clear quantum-classical correspondence via Fourier transformation technique[15].

Thus, in the current paper (Part I), we focus on the radial dependence of the mean field potential (effect of surface diffuseness, described by the  $l^2$  term in the Nilsson model) and examine the shell structures systematically as functions of deformation and surface diffuseness. As pointed out by Tajima et al., spin-orbit coupling play also an important role in prolate-shape dominance. The effect of spin-orbit coupling will be discussed in the forthcoming paper (Part II).

This paper is organized as follows. In Sect. II, we discuss the quantum and classical properties of power-law potential model. The scaling properties of the model are described and the Fourier transformation techniques are formulated. In Sect. III, quantum mechanical density of states and shell structures in spherical power-law potential are examined. Some analytic expressions for periodic orbit bifurcations and semiclassical formula are given, and quantum-classical correspondence is discussed. It is shown that bifurcations of circular orbit play essential role in unique shell structures which appear at several values of radial parameter  $\alpha$ . In Sect. IV, shell structures are examined against spheroidal deformation parameter. Semiclassical origin of prolate-oblate asymmetry in deformed shell structures and that of superdeformed shell structure are investigated. Special attention is paid on what we call ‘‘bridge orbit bifurcations’’. Section V is devoted to summary and conclusion.

## II. THE POWER-LAW POTENTIAL MODEL

### A. Definition of the model

It is known that the central part of the nuclear mean field potential is approximately given by the Woods-Saxon (WS) model

$$V_{\text{WS}}(r) = -\frac{W}{1 + \exp\{(r - R_A)/a\}}. \quad (2.1)$$

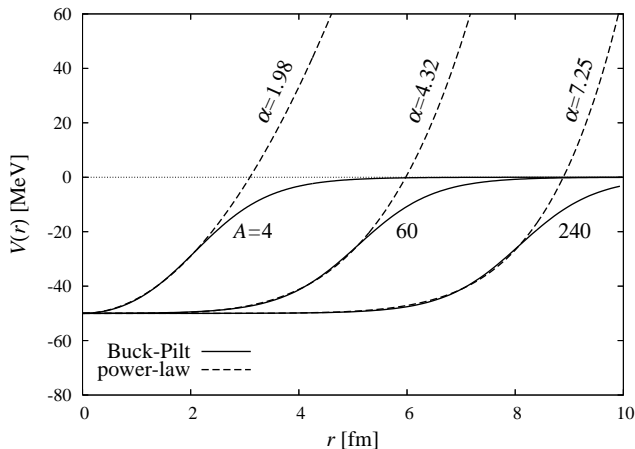


FIG. 1. Profiles of power-law potentials (2.3) fitted to the Buck-Pilt potentials (2.2) for mass numbers  $A = 4, 60$  and  $240$ . Values of radial parameter  $\alpha$  are determined by Eq. (2.5).

The depth of the potential is  $W \simeq 50$  MeV, surface diffuseness is  $a \simeq 0.7$  fm and nuclear radius is  $R_A \sim 1.3A^{1/3}$  fm for a nucleus with mass number  $A$  [16]. The singularity of the potential (2.1) at the origin can be removed by replacing WS potential with Buck-Pilt (BP) potential[17]

$$V_{\text{BP}}(r) = -W \frac{1 + \cosh(R_A/a)}{\cosh(r/a) + \cosh(R_A/a)}. \quad (2.2)$$

By using BP potential whose radial profile is essentially equivalent to the WS potential, one can consider semiclassical quantization without concerning about the singularity in classical orbits[13, 14]. For small  $A$ , the inner region ( $r < R_A$ ) of these potentials can be approximated by harmonic oscillator (HO). For large  $A$ , these potentials are flat ( $V \approx -W$ ) around  $r = 0$  and sharply approaches zero around the surface, which looks more similar to square well potential. In Ref. [9], shell energy of deformed WS potentials are compared with those for HO and infinite square-well (cavity) potentials. Deformed shell structures in WS model are similar to those of HO model for light nuclei, while they are more like those of cavity model for medium-mass to heavy nuclei. Our aim is to understand the above transition of deformed shell structure from the view point of quantum-classical correspondence. For this purpose, we take the radial dependence of the potential as  $r^\alpha$ , which smoothly connect HO ( $\alpha = 2$ ) and cavity ( $\alpha = \infty$ ) potentials by varying the radial parameter  $\alpha$ :

$$V_{\text{BP}}(r) \approx V_\alpha(r) = -W + \frac{W}{2} \left( \frac{r}{R_A} \right)^\alpha. \quad (2.3)$$

This *power-law potential*  $V_\alpha$ , having simple radial profile, is easy to treat in both quantum and classical mechanics in comparison with WS/BP model. The inner region ( $r \lesssim R$ ) of BP potential is nicely approximated by the power-law potential (see Fig. 1).

In Fig. 1, the radial parameter  $\alpha$  is determined so that the power-law potential best fit the inner region ( $r < R_A$ ) of BP potential. As a simple local matching, one may equate the

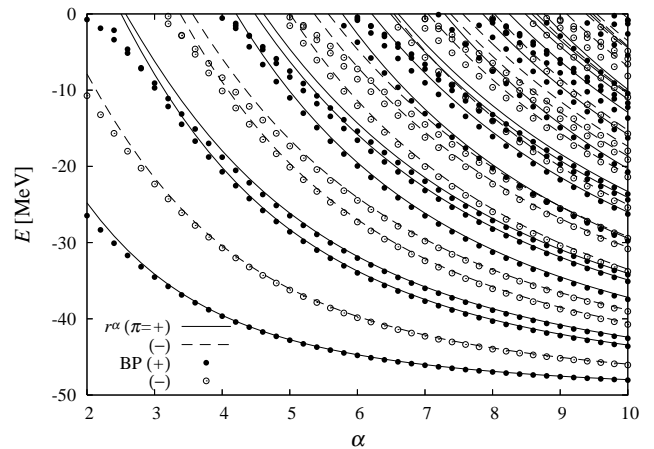


FIG. 2. Single-particle spectra for spherical power-law ( $r^\alpha$ ) potential and Buck-Pilt (BP) potential as functions of radial parameter  $\alpha$ . Positive and negative parity levels ( $\pi = \pm$ ) are respectively plotted with solid and dashed lines for power-law potential and with filled and open dots for BP potential. For the levels of BP model (2.1), nuclear radius  $R_A$  is determined by Eq. (2.6) as a function of  $\alpha$ .

derivatives of two potentials at the nuclear surface  $r = R_A$ , which gives (for  $a \ll R_A$ )

$$\alpha \sim R_A/2a. \quad (2.4)$$

Thus, the radial parameter  $\alpha$  controls the surface diffuseness. For a global fitting, we take more elaborate way which minimize volume integral of squared potential difference inside the nuclear radius  $R_A$ ;

$$\frac{d}{d\alpha} \int_0^{R_A} dr r^2 \left\{ V_\alpha(r; A) - V_{\text{BP}}(r; A) \right\}^2 = 0. \quad (2.5)$$

The value of  $\alpha$  numerically obtained by Eq. (2.5) has an approximately linear dependence on  $R_A/a$ ,

$$\alpha \sim -0.62 + 0.68 R_A/a, \quad (2.6)$$

which has qualitatively similar dependence on surface diffuseness  $a$  as the result of local fitting (2.4).

Fig. 2 compares single-particle level diagrams for BP and power-law potential models as functions of radial parameter  $\alpha$ . We use the relation (2.6) to determine  $R_A$  for WS potential as function of  $\alpha$ . Although the difference of two potentials becomes significant at  $E \gtrsim -20$  MeV, the quantum spectra for these models show fairly nice agreements up to Fermi energy ( $E_F \sim -8$  MeV) in wide range of radial parameter  $\alpha$  (see Fig. 2). Since most of the classical orbits have non-zero angular momentum and they don't reach the outer bound of the potential due to centrifugal potential, the difference of the two potentials at  $r > R_A$  are hindered in semiclassical quantization and it might not cause much differences in the quantum spectra up to rather high energy.

Thus, we can employ this power-law potential model for the study of realistic shell structures of stable nuclei from light to heavy regions. For unstable nuclei, difference of the potentials at  $r > R_A$  and the effect of coupling to continuum states might become significant.

TABLE I. Values of radial parameter  $\alpha$ , length unit  $R$  and energy unit  $U$  of power-law potential (2.7) for nuclei with mass number  $A$ . Nuclear radius  $R_A = 1.3A^{1/3}$  fm, potential depth  $W = 50$  MeV, surface diffuseness  $a = 0.7$  fm, nucleon mass  $m = 938$  MeV/ $c^2$  and the relation (2.6) are used.

$A$	$\alpha$	$R$ [fm]	$U$ [MeV]
20	2.80	2.32	3.32
100	5.23	3.93	1.14
200	6.75	5.06	0.72

### B. Scaling properties

There is a great advantage to replace WS/BP potential with the power-law potential. The power-law potential has useful scaling properties, which highly simplifies our semiclassical analysis. In the following, we eliminate the constant term  $-W$  in Eq. (2.3) and consider the Hamiltonian for a particle of mass  $m$  moving in the deformed power-law potential as

$$H(\mathbf{p}, \mathbf{r}) = \frac{p^2}{2m} + U \left[ \frac{r}{Rf(\theta, \varphi)} \right]^\alpha. \quad (2.7)$$

Here,  $R$  and  $U$  are constants having dimension of length and energy, respectively. The dimensionless function  $f(\theta, \varphi)$  determines the shape of the equi-potential surface, and it is normalized to satisfy volume conservation condition

$$\frac{1}{4\pi} \int f^3(\theta, \varphi) d\Omega = 1, \quad (2.8)$$

which guarantees the volume surrounded by equi-potential surface to be independent of deformation. Under suitable scale transformation of coordinates, energy eigenvalue equation is transformed into a dimensionless form

$$\left[ -\frac{1}{2} \nabla_u^2 + \left( \frac{u}{f(\theta, \varphi)} \right)^\alpha \right] \psi(\mathbf{u}) = e \psi(\mathbf{u}), \quad (2.9)$$

by the choice  $U = \hbar^2/mR^2$  (note that the value of  $U$  can be taken arbitrarily, since the potential can be still adjusted by another parameter  $R$ ), and dimensionless coordinates  $\mathbf{u}$  and energy  $e$  defined by

$$\mathbf{u} = \frac{\mathbf{r}}{R}, \quad e = \frac{E}{U}. \quad (2.10)$$

$\nabla_u^2$  represents Laplacian with respect to the coordinate  $\mathbf{u}$ . Since Eq. (2.9) does not include constants such as  $m$ ,  $U$ ,  $R$  and  $\hbar$ , one can consider quantum eigenvalue problem independently on those values. Their absolute values are determined by fitting to the BP potential through the relation

$$U \left( \frac{R_A}{R} \right)^\alpha = \frac{W}{2}.$$

The values of  $\alpha$ ,  $R$  and  $U$  for several  $A$  are listed in Table I.

The scaling property of the system is particularly advantageous in the analysis of classical dynamics. Since the potential is a homogeneous function of coordinates, Hamilton's

equations of motion have the invariance under the following scale transformation

$$(\mathbf{p}, \mathbf{r}, t) \rightarrow (c^{1/2} \mathbf{p}, c^{1/\alpha} \mathbf{r}, c^{1/\alpha - 1/2} t) \quad \text{as} \quad E \rightarrow cE. \quad (2.11)$$

Therefore, classical phase space structure is independent of energy. A phase space trajectory  $(\mathbf{r}_0(t), \mathbf{p}_0(t))$  at energy  $E_0$  is transformed to a trajectory at different energy  $E$  by

$$\begin{aligned} \mathbf{r}(t) &= \left( \frac{E}{E_0} \right)^{1/\alpha} \mathbf{r}_0(t'), & \mathbf{p}(t) &= \left( \frac{E}{E_0} \right)^{1/2} \mathbf{p}_0(t'), \\ \text{with} \quad t &= \left( \frac{E}{E_0} \right)^{1/\alpha - 1/2} t'. \end{aligned} \quad (2.12)$$

Thus we have the same set of periodic orbits in arbitrary energy surface related through the above scale transformation. In the following, we set the reference energy at  $E_0 = U$ . The action integral along a certain periodic orbit  $\beta$  is expressed as

$$S_\beta(E) = \oint_{\beta(E)} \mathbf{p} \cdot d\mathbf{r} = S_\beta(U) \left( \frac{E}{U} \right)^{1/2 + 1/\alpha} \equiv \hbar \tau_\beta \mathcal{E}. \quad (2.13)$$

In the last equation, we define dimensionless ‘‘scaled energy’’  $\mathcal{E}$  and ‘‘scaled period’’  $\tau_\beta$  of periodic orbit  $\beta$  by

$$\mathcal{E} = \left( \frac{E}{U} \right)^{1/2 + 1/\alpha}, \quad \tau_\beta = \frac{S_\beta(U)}{\hbar}. \quad (2.14)$$

The ordinary (non-scaled) period of the orbit  $\beta$  is then given by

$$T_\beta = \frac{\partial S_\beta(E)}{\partial E} = \frac{d\mathcal{E}}{dE} \hbar \tau_\beta. \quad (2.15)$$

As one will see in the following part, it is convenient to express periodic-orbit quantities in terms of  $\mathcal{E}$  and  $\tau$  in place of  $E$  and  $T$ . In HO-type potentials ( $\alpha = 2$ ),  $\mathcal{E}$  and  $\tau$  are proportional to ordinary energy  $E$  and period  $T$ , respectively. In cavities ( $\alpha = \infty$ ), they are proportional to momentum  $p$  and orbit length  $L$ , respectively.

### C. Semiclassical level density

Let us consider the single-particle level density for the Hamiltonian (2.7). Average level density  $\bar{g}(E)$  is given by Thomas-Fermi (TF) theory

$$\begin{aligned} g_{TF}(E) &= \frac{1}{(2\pi\hbar)^3} \int d\mathbf{p} d\mathbf{r} \delta(E - H(\mathbf{p}, \mathbf{r})) \\ &= \frac{2\sqrt{2}}{\pi\alpha} \mathbf{B} \left( \frac{3}{\alpha}, \frac{3}{2} \right) \frac{\mathcal{E}^3}{E}, \end{aligned} \quad (2.16)$$

which is independent of deformation under volume conservation condition (2.8).  $\mathbf{B}(s, t)$  represents Euler's beta function defined by

$$\mathbf{B}(s, t) = \int_0^1 x^{s-1} (1-x)^{t-1} dx.$$

By transforming energy  $E$  to a scaled energy  $\mathcal{E}$ , one obtains the scaled-energy level density

$$g(\mathcal{E}) = \frac{dE}{d\mathcal{E}} g(E) = \frac{2\alpha}{2+\alpha} \frac{E}{\mathcal{E}} g(E) \quad (2.17)$$

Using (2.16), the average part is given by

$$\bar{g}(\mathcal{E}) = \frac{2\sqrt{2}}{\pi} \text{B} \left( 1 + \frac{3}{\alpha}, \frac{3}{2} \right) \mathcal{E}^2 \quad (2.18)$$

Correction to the TF density is obtained by the extended Thomas-Fermi (ETF) theory[18, 19]

$$\begin{aligned} \bar{g}_{\text{ETF}}(E) &= \bar{g}_{\text{TF}}(E) - \frac{1}{96\pi^2} \left( \frac{2m}{\hbar^2} \right)^{1/2} \\ &\times \frac{\partial}{\partial E} \int d\mathbf{r} \theta(E - V) \frac{\nabla^2 V}{(E - V)^{1/2}} \end{aligned} \quad (2.19)$$

For spherical case, we have the expression

$$\bar{g}_{\text{ETF}}(\mathcal{E}) = \bar{g}_{\text{TF}}(\mathcal{E}) - \frac{\alpha+1}{12\sqrt{2}\pi} \text{B} \left( 1 + \frac{1}{\alpha}, \frac{1}{2} \right) \quad (2.20)$$

and the average number of levels up to energy  $E$  ( $\mathcal{E}$ ) is given by

$$\begin{aligned} \bar{N}(\mathcal{E}) &= \frac{2\sqrt{2}}{3\pi} \text{B} \left( 1 + \frac{3}{\alpha}, \frac{3}{2} \right) \mathcal{E}^3 \\ &- \frac{\alpha+1}{12\sqrt{2}\pi} \text{B} \left( 1 + \frac{1}{\alpha}, \frac{1}{2} \right) \mathcal{E}. \end{aligned} \quad (2.21)$$

In Fig. 3, quantum-mechanically calculated coarse-grained level density

$$g(\mathcal{E}) = \sum_i \frac{1}{\sqrt{2\pi\Delta\mathcal{E}}} \exp \left[ -\frac{1}{2} \left( \frac{\mathcal{E} - \mathcal{E}_i}{\Delta\mathcal{E}} \right)^2 \right] \quad (2.22)$$

and number of levels

$$N(\mathcal{E}) = \sum_i \theta(\mathcal{E} - \mathcal{E}_i), \quad (2.23)$$

are compared with ETF results. One sees that ETF (TF) correctly describes the average properties of quantum results. In these plots, difference between ETF and TF is invisibly small.

Next we consider the fluctuating part by the use of semiclassical periodic-orbit theory[19]. Let us rewrite the trace formula (1.1) using scaled energy and scaled periods. Semiclassical formula for scaled-energy level density is expressed as

$$g(\mathcal{E}) = \bar{g}(\mathcal{E}) + \sum_{\beta} \sum_{n=1}^{\infty} A_{n\beta}(\mathcal{E}) \cos \left( n\tau_{\beta}\mathcal{E} - \frac{\pi}{2} \nu_{n\beta} \right). \quad (2.24)$$

In the Hamiltonian system with no continuous symmetry, all the periodic orbits are isolated from each other. For a system with continuous symmetry, e.g., a particle moving in axially symmetric potential, generic periodic orbits form continuous family with respect to the symmetry transformation and they

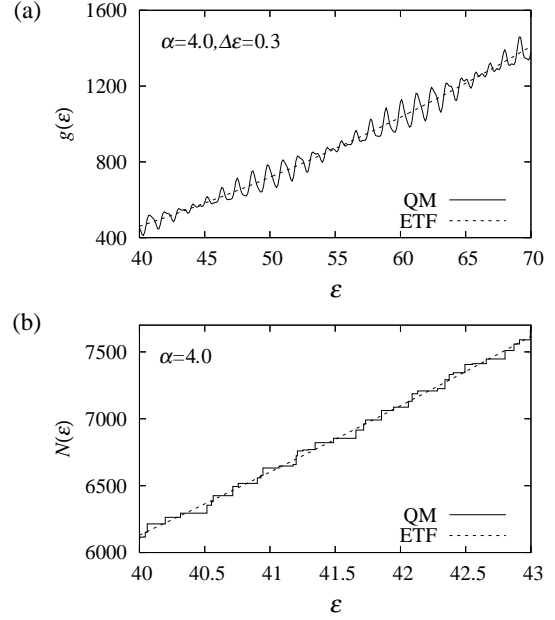


FIG. 3. Comparison of quantum (QM: solid line) and semiclassical (ETF: broken line) results for spherical power-law potential with  $\alpha = 4.0$ . In the upper panel (a), coarse-grained quantum level density (2.22) with smoothing width  $\Delta\mathcal{E} = 0.3$ , and ETF level density (2.20) are displayed. In the lower panel (b), number of quantum levels below scaled energy  $\mathcal{E}$  (2.23) and ETF average number of levels (2.21) are displayed.

are called *degenerate orbit*. For an *isolated orbit*  $\beta$  with  $n$  repetitions, amplitude factor is given by the standard Gutzwiller formula[1, 19],

$$A_{n\beta} = \frac{T_{\beta}}{\pi\hbar\sqrt{|\det(\mathbf{I} - \mathbf{M}_{\beta}^n)|}} \frac{dE}{d\mathcal{E}} = \frac{\tau_{\beta}}{\pi\sqrt{|\det(\mathbf{I} - \mathbf{M}_{\beta}^n)|}}. \quad (2.25)$$

In the last equation, we used Eq. (2.15).  $\mathbf{M}_{\beta}$  represents the monodromy matrix[19, 20], which is a linearized Poincaré map defined by

$$\mathbf{M}_{\beta} = \frac{\partial(\mathbf{r}_{\perp}(T_{\beta}), \mathbf{p}_{\perp}(T_{\beta}))}{\partial(\mathbf{r}_{\perp}(0), \mathbf{p}_{\perp}(0))}, \quad (2.26)$$

where  $(\mathbf{r}_{\perp}(t), \mathbf{p}_{\perp}(t))$  are the local coordinates and momenta perpendicular to the periodic orbit  $\beta$  as functions of time  $t$ , and  $T_{\beta}$  is the period of the orbit.

In a two-dimensional autonomous Hamiltonian system, monodromy matrix  $\mathbf{M}$  is a  $(2 \times 2)$  real and symplectic matrix,

$$\mathbf{M}\mathbf{J}\mathbf{M}^T = \mathbf{J}, \quad \mathbf{J} = \begin{pmatrix} 0 & 1 \\ -1 & 0 \end{pmatrix},$$

and its eigenvalues appear in one of the following three forms[19, 20]:

- (a)  $(e^u, e^{-u})$ : hyperbolic with no reflection  
 $\text{Tr}\mathbf{M} = 2 \cosh u > 2$
- (b)  $(e^{iv}, e^{-iv})$ : elliptic  
 $\text{Tr}\mathbf{M} = 2 \cos v, \quad |\text{Tr}\mathbf{M}| \leq 2$

(c)  $(-e^u, -e^{-u})$ : hyperbolic with reflection  
 $\text{Tr}\mathbf{M} = -2 \cosh u < -2$

The orbit is stable in the case (b) and otherwise unstable, and stability of the orbit is determined by the trace of monodromy matrix. The stability factor in (2.25) is also determined by the trace of monodromy matrix:

$$\det(\mathbf{I} - \mathbf{M}_\beta) = 2 - \text{Tr}\mathbf{M}_\beta. \quad (2.27)$$

The eigenvalues of  $\mathbf{M}$  (and therefore  $\text{Tr}\mathbf{M}$ ) are independent of a choice of Poincaré surface or a choice of canonical variables. These eigenvalues continuously vary as deformation changes, and it happens that they become unity at certain values of deformation, namely,  $u = 0$  in (a) or  $v = 0$  in (b). At those deformations, Poincaré map acquires a new fixed point in the direction of eigenvector  $\delta Z_1$  belonging to the unit eigenvector:

$$\mathbf{M}\delta Z_1 = \delta Z_1. \quad (2.28)$$

In this way, periodic orbit bifurcation occurs at  $\text{Tr}\mathbf{M} = 2$ . The number of new emerging orbits is dependent on the type of the bifurcation[21]. When a stable (unstable) orbit undergoes *pitchfork* bifurcation, it turns unstable (stable) and a new stable (unstable) orbit emerges from it. When a stable orbit undergoes *period-doubling* bifurcation, a pair of stable and unstable orbits will emerge.

In a three-dimensional Hamiltonian system, the size of monodromy matrix becomes  $(4 \times 4)$ . Under axial symmetry, periodic orbits degenerate with respect to the rotation, and the monodromy matrix has unit eigenvalue corresponding to the direction of the rotation. Thus, by removing the rotational degrees of freedom, stability of the orbit is described by  $(2 \times 2)$  symmetry-reduced monodromy matrix, and it has the same properties as in the two-dimensional case. For such degenerate orbits in the system with continuous symmetry, the trace formula is modified by what is called *extended Gutzwiller theory*[19, 22]. The amplitude factor for the degenerate orbit is proportional to the stability factor similar to that in (2.25), but with symmetry-reduced monodromy matrix  $\tilde{\mathbf{M}}_\beta$ . For fully degenerate orbits in integrable system, one can use Berry-Tabor formula[23].

In general, the stability factor  $|\det(\mathbf{I} - \tilde{\mathbf{M}}_\beta^n)|^{-1/2}$  has strong dependence on the deformation parameter, and is responsible for the sensitivity of shell structures upon deformations. The divergence of the Gutzwiller amplitude (2.25) based on standard stationary phase method can be remedied by improved treatment of trace integral in phase space (e.g., uniform approximations[24–26] and improved stationary-phase method[12, 27]) and one can obtain finite amplitude through the bifurcation processes. Those amplitudes sometimes show strong enhancement around the bifurcation points, since the monodromy matrix has a unit eigenvalue there, and a local family of quasi-periodic orbits are formed in direction of the eigenvector  $\delta Z_1$  belonging to the unit eigenvalue, which make coherent contribution to the level density.

One should however note that the above enhancement is not always found for every bifurcations. The significance of bifurcation depends on the normal form parameters which describe nonlinear dynamics around the periodic orbit at the bifurcation points. In Ref. [28], uniform approximation remedies

the divergence problems which one encounters at bifurcation points in standard stationary phase method, but the obtained amplitude show no enhancement around there. In Ref. [29], we found very strong enhancement of amplitude around the bifurcation point for one certain orbit, but the same type of bifurcation in another orbit shows no enhancement. In our previous studies, we have shown that significant growth of shell effect at a certain deformation is related with bifurcations of *simple short* periodic orbits[11, 12, 27, 29, 30].

#### D. Fourier transformation technique

Fourier transformation technique is especially useful in studying classical-quantum correspondence in the system with scale invariance. Let us consider the Fourier transform of scaled-energy level density

$$F(\tau) = \int g(\mathcal{E}) e^{i\tau\mathcal{E}} e^{-\frac{1}{2}(\gamma\mathcal{E})^2} d\mathcal{E}. \quad (2.29)$$

In the integrand, Gaussian damping factor is included in order to exclude the level density at high energy  $\gamma\mathcal{E} \gg 1$  where the numerically obtained single-particle spectra are not in a good precision.

By inserting the quantum level density  $g(\mathcal{E}) = \sum_n \delta(\mathcal{E} - \mathcal{E}_n)$  into Eq. (2.29), one obtains

$$F^{\text{qm}}(\tau) = \sum_{\mathcal{E}_n < \mathcal{E}_{\text{max}}} e^{i\tau\mathcal{E}_n - \frac{1}{2}(\gamma\mathcal{E}_n)^2}, \quad (2.30)$$

which can be easily calculated using quantum mechanically calculated energy eigenvalues  $\{\mathcal{E}_n\}$ . On the other hand, by inserting the semiclassical level density (2.24), one formally has the expression

$$F^{\text{cl}}(\tau) = \bar{F}(\tau) + \pi \sum_{n\beta} e^{i\pi\mu_{n\beta}/2} A_{n\beta}(-i\partial_\tau) \delta_\gamma(\tau - n\tau_\beta). \quad (2.31)$$

Here,  $\delta_\gamma(z)$  represents a normalized Gaussian with width  $\gamma$

$$\delta_\gamma(z) = \frac{1}{\sqrt{2\pi}\gamma} e^{-\frac{z^2}{2\gamma^2}}, \quad (2.32)$$

which coincides with Dirac's delta function in the limit  $\gamma \rightarrow 0$ . Thus,  $F(\tau)$  should be a function possessing successive peaks at the scaled periods of classical periodic orbits  $\tau = n\tau_\beta$ . (In Eq. (2.31), the argument  $\mathcal{E}$  of the amplitude  $A(\mathcal{E})$  is formally replaced with differential operator  $-i\partial_\tau$ . For isolated orbit, amplitude is a constant and the corresponding term in (2.31) becomes a simple gaussian. For degenerate family of degeneracy  $\mathcal{K}$ , amplitude is proportional to  $\mathcal{E}^{\mathcal{K}/2}$  and the peak might not exactly centered at the scaled action.) Therefore, by calculating Fourier transform of quantum mechanical level density, one can extract information on the significance of each periodic orbits contributing to semiclassical level density.

The parameter  $\gamma$  implies the resolution of the periodic orbit in the Fourier transform. For a better resolution, larger number of good quantum energy levels (up to  $\mathcal{E}_{\text{max}} \gtrsim 2/\gamma$ ) are required.

### III. SPHERICAL POWER-LAW POTENTIALS

#### A. Quantum spectra and shell structures

Let us first examine the quantum spectra in spherical power-law potentials. In case of  $\alpha = 2$  (isotropic harmonic oscillator), energy levels with different angular momentum degenerate due to dynamical SU(3) symmetry. With increasing  $\alpha$ , these degeneracies are resolved and shell effect becomes weaker. However, new types of prominent shell structures will emerge at certain values of  $\alpha$ . The shell structure, a fluctuation in single-particle spectrum, brings about a fluctuation in energy of nuclei as functions of constituent nucleon numbers. This fluctuation part, which we call *shell energy*, is calculated by removing the smooth part from a sum of single-particle energies by means of Strutinsky method[31, 32].

Figure 4 displays oscillating part of the coarse-grained scaled-energy level density  $\delta g(\mathcal{E})$  divided by  $\mathcal{E}$  and shell energies  $E_{\text{sh}}$  for several values of  $\alpha$ . In each panel of Fig. 4(a), results with two different values of smoothing width  $\Delta\mathcal{E}$  are shown. With  $\Delta\mathcal{E} = 0.12$ , some fine structures can be examined. One sees characteristic patterns of oscillations in results for  $\alpha = 4.0$  and 5.0: the former has sub-shell structures with 3 bumps per each major shell, and the latter has that with 2 bumps per each major shell. Such sub-shell structures are not evident for  $\alpha = 8.0$ . With  $\Delta\mathcal{E} = 0.24$ , only the gross-most structure is extracted. One sees that the magnitude of major shell effect is considerably enhanced at  $\alpha = 8.0$ . These sub-shell structures are obvious in level densities and their effect to shell energies are also noticeable. These plots are extended to large  $\mathcal{E}$  and  $N$  (far beyond the region of existing nuclei, but may meaningful for metallic clusters), where the above sub-shell structures become more evident. The sub-shell bumps for  $\alpha = 4.0$  and 5.0 in shell energies are not very prominent in existing nuclear region and they might disappear, e.g., after including the spin-orbit coupling, but the pronounced shell effect for  $\alpha \sim 8.0$  might survive and be responsible for enhancement of shell effect in real nuclei around medium-mass to heavy region.

In the following subsections, we will show that the above unique shell structures can be explained as the effect of different types of periodic orbit bifurcations which take places around the above values of  $\alpha$ .

#### B. Classical periodic orbits

In spherical power-law potential model, several simple analytic descriptions for the properties of the periodic orbits are available. Taking the orbits in  $(x, y)$  plane and putting the  $z$ -component of angular momentum to  $l_z = K$ , 2-dimensional effective Hamiltonian in polar coordinates is written as

$$H = \frac{1}{2}p_r^2 + V_{\text{eff}}(r; K), \quad V_{\text{eff}}(r; K) = r^\alpha + \frac{K^2}{2r^2} \quad (3.1)$$

Circular orbit  $r(t) = r_c$  (denoted by C) satisfies the condition

$$\left( \frac{\partial V_{\text{eff}}}{\partial r} \right)_{r_c} = 0, \quad (3.2)$$

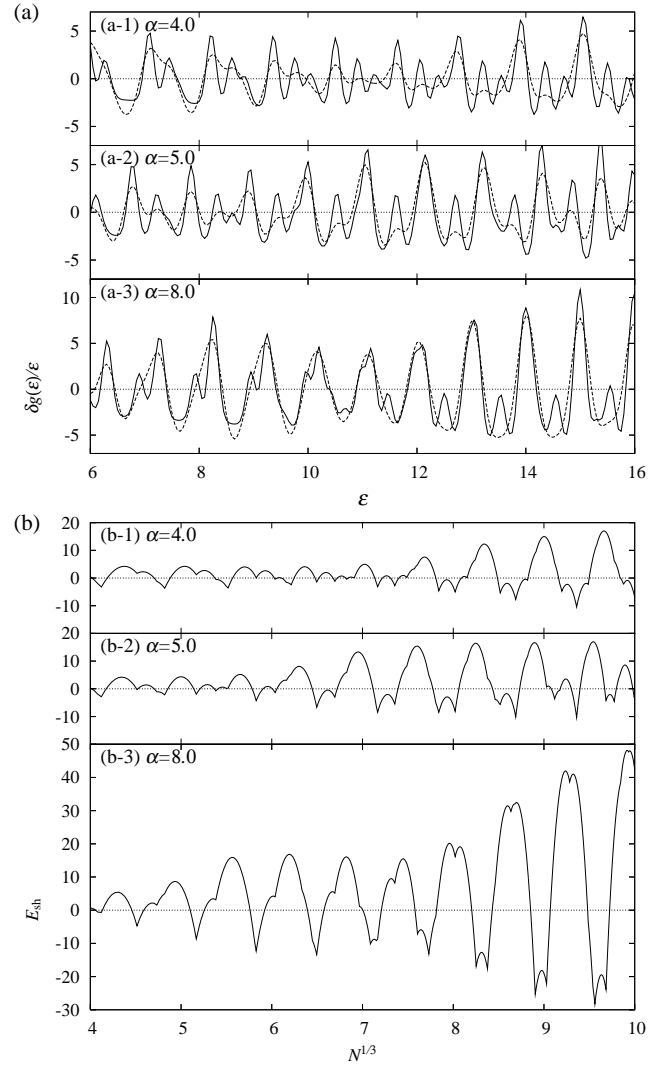


FIG. 4. (a) Oscillating part of the coarse-grained scaled-energy level density  $\delta g(\mathcal{E})$  divided by  $\mathcal{E}$  in spherical power-law potential model with  $\alpha = 4.0, 5.0$  and  $8.0$ . Solid and dashed lines show results with smoothing width  $\Delta\mathcal{E} = 0.12$  and  $0.24$ , respectively. (b) Shell energy as functions of the cubic root of particle number, which is either of neutron or proton, taking account of the spin degeneracy factor.

from which one obtains, for energy  $E$ ,

$$r_c = \left( \frac{2E}{2+\alpha} \right)^{1/\alpha}. \quad (3.3)$$

and the angular frequency

$$\omega_c = \frac{K}{r_c^2} = \sqrt{\alpha} \left( \frac{2E}{2+\alpha} \right)^{\frac{1}{2} - \frac{1}{\alpha}}. \quad (3.4)$$

The circular orbit is stable, and  $r(t)$  of the orbits in vicinities of the circular orbit oscillate around  $r_c$  with angular frequency

$$\Omega_c = \sqrt{\left( \frac{\partial^2 V_{\text{eff}}}{\partial r^2} \right)_{r_c}} = \sqrt{\alpha(\alpha+2)} \left( \frac{2E}{2+\alpha} \right)^{\frac{1}{2} - \frac{1}{\alpha}}. \quad (3.5)$$

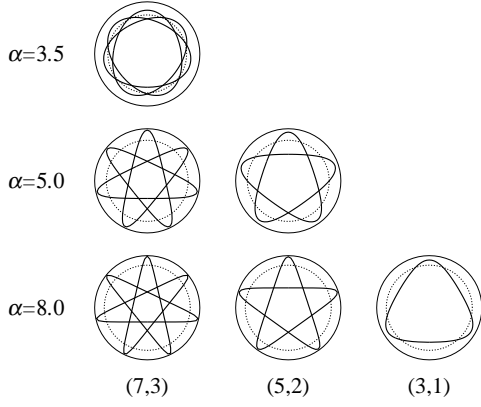


FIG. 5. Some short periodic orbits  $(n, m)$  in spherical power-law potentials. They emerge from the circular orbit (shown in broken lines) via period- $m$  bifurcations.

Bifurcations occur when the ratio of those two frequencies  $\omega_c$  and  $\Omega_c$  becomes rational, namely,

$$\frac{\Omega_c}{\omega_c} = \sqrt{\alpha + 2} = \frac{n}{m} \quad (3.6)$$

for period- $m$  bifurcation. Here, a new orbit which oscillates  $n$  times in radial direction when it rotates  $m$  times along the orbit C emerges from  $m$ -th repetition of orbit C. The values of  $\alpha$  at such bifurcations are given by

$$\alpha = \frac{n^2}{m^2} - 2 \quad (3.7)$$

$$= \begin{cases} 2, 7, 14, \dots & (m=1) \\ \left(\frac{8}{4}\right), \frac{17}{4}, \left(\frac{28}{4}\right), \frac{41}{4}, \dots & (m=2) \\ \left(\frac{18}{9}\right), \frac{31}{9}, \frac{46}{9}, \left(\frac{63}{9}\right), \frac{82}{9}, \frac{103}{9}, \dots & (m=3) \\ \vdots & \vdots \end{cases}$$

Figure 5 shows some periodic orbits  $(n, m)$  emerge from the circular orbit via period-multiplying bifurcations of circular orbit C.

In Fig. 6 we show Fourier amplitudes of quantum level density (2.30) plotted as functions of scaled period  $\tau$  for several values of  $\alpha$ . For  $\alpha = 4.0$ , one sees a large peak at  $\tau \sim 17$ . This peak corresponds to 3rd repetitions of circular orbit, 3C, as well as orbit (7,3) bifurcated from 3C at  $\alpha = 31/9 = 3.44$ . Since these orbits have periods about three times as long as primitive circular orbit, the interference of their contribution to the semiclassical level density will show a shell structure such that a major shell is modulated by a small oscillations having triple frequency. Thus, the appearance of subshell structure found in Fig. 4(a) is understood as a result of bifurcation enhancement effect of orbit (7,3). For  $\alpha = 5.0$ , the highest peak at  $\tau = 12$  corresponds to the 2nd repetitions of circular orbit, 2C, as well as orbit (5,2) bifurcated from 2C at  $\alpha = 4$ . In the lower panel, peak at  $\tau \sim 7$  corresponds to the primitive circular orbit C and orbit (3,1) bifurcated from C at

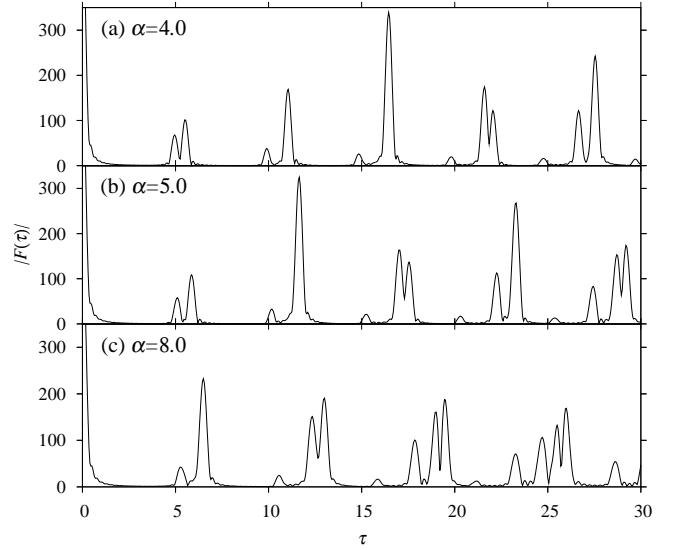


FIG. 6. Moduli of Fourier transforms of quantum level density (2.30) plotted as functions of scaled period  $\tau$  for  $\alpha = 4.0, 5.0,$  and  $8.0$ .

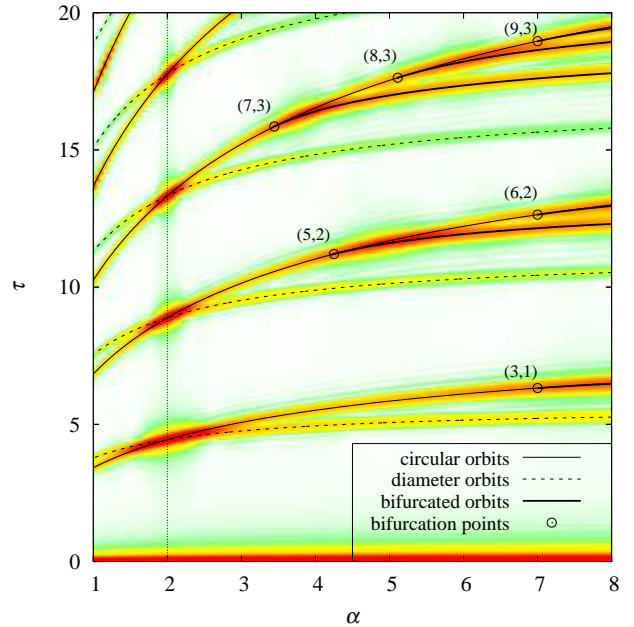


FIG. 7. (color online) Gray-scale plot of Fourier transform of quantum level density (2.30) as function of radial parameter  $\alpha$  and scaled period  $\tau$ . Modulus of the Fourier transform  $|F(\tau)|$  has large value at dark region. Scaled periods of classical periodic orbits  $\tau_\beta(\alpha)$  are also shown with lines as functions of  $\alpha$ . Bifurcation points are indicated by open circles.

$\alpha = 7$ . Shell structures found in Fig. 4(b) and (c) panels of Fig. 4 can be understood, just in the same way as upper panel, as the bifurcation enhancement effect of orbit (5,2) and (3,1), respectively.

Figure 7 shows a two-dimensional gray-scale plot of quantum mechanical Fourier amplitude  $|F(\tau; \alpha)|$  as a function of radial parameter  $\alpha$  and scaled period  $\tau$ . Scaled periods of

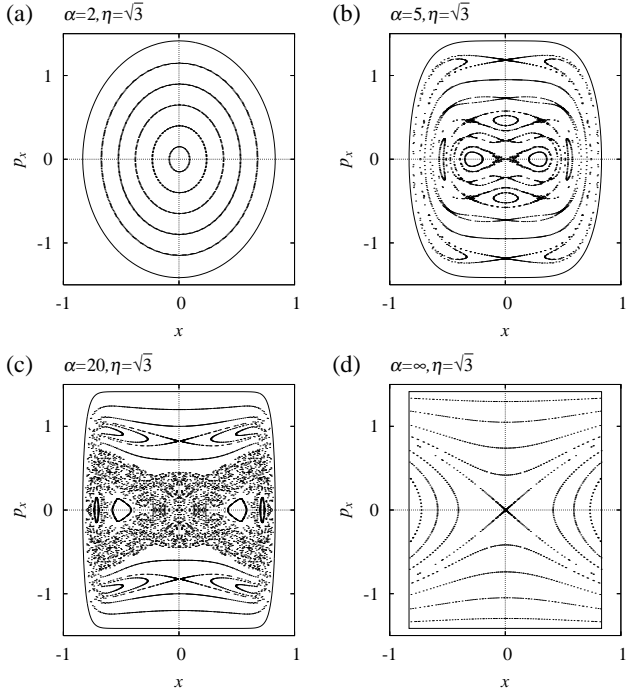


FIG. 8. Poincaré surface of section  $\{(x, p_x)|z=0\}$  for meridian-plane orbits in spheroidal-shape potentials with axis ratio  $\eta = \sqrt{3}$  ( $\delta \approx 0.49$ ) and with several values of radial parameter  $\alpha$ . The origin ( $x = p_x = 0$ ) corresponds to the orbit Z, and the outer boundary corresponds to the orbit X.

classical periodic orbits are also drawn as functions of  $\alpha$ . We see nice agreements between quantum Fourier transforms and classical periodic orbits. The Fourier peaks associated with periodic orbits are strongly enhanced around their bifurcation points indicated by open circles. This clearly illustrates the significance of periodic-orbit bifurcations to the enhancement of shell effect.

#### IV. SPHEROIDAL DEFORMATIONS

##### A. Shape parametrization and quantum spectra

Axially-symmetric anisotropic harmonic oscillator potential system is integrable, and it has spheroidal equi-potential surface. It is known that spheroidal deformed cavity (infinite well potential) system is also integrable. For spheroidal deformation, shape function is expressed as

$$f(\theta) = \sqrt{\frac{r^2/R_0^2}{\frac{x^2+y^2}{R_\perp^2} + \frac{z^2}{R_z^2}}} = \left[ \frac{\sin^2 \theta}{(R_\perp/R_0)^2} + \frac{\cos^2 \theta}{(R_z/R_0)^2} \right]^{-1/2} \quad (4.1)$$

where  $R_z$  and  $R_\perp$  represent lengths of semiaxes of the spheroid which are parallel and perpendicular to the symmetry axis ( $z$ -axis), respectively. Taking account of the volume conservation

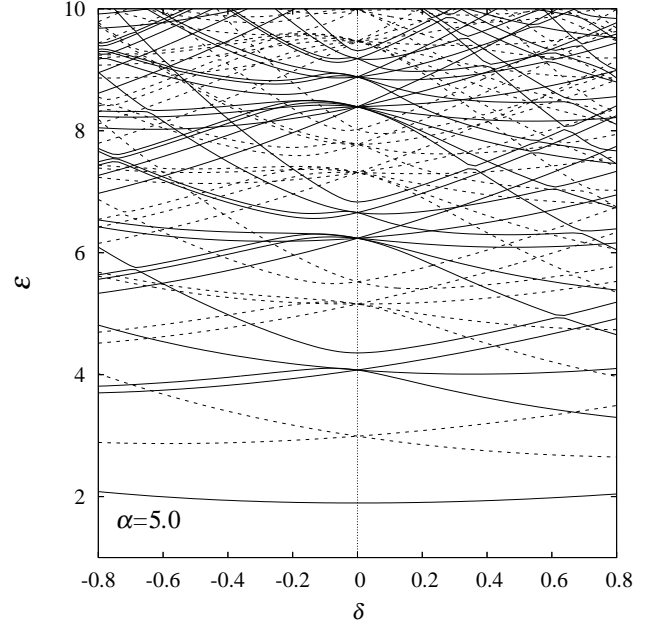


FIG. 9. Single-particle level diagram for Hamiltonian (2.7) with spheroidal deformation (4.1). Scaled-energy levels are plotted as functions of deformation parameter  $\delta$  defined by Eq. (4.2). Solid and broken lines represents levels with even and odd parities, respectively.

condition  $R_\perp^2 R_z^2 = R_0^3$ , we define the deformation parameter  $\delta$  as

$$R_\perp = R_0 e^{-\delta/3}, \quad R_z = R_0 e^{2\delta/3}. \quad (4.2)$$

It is related with the axis ratio  $\eta = R_z/R_\perp$  by  $\eta = e^\delta$ . Spherical shape  $\eta = 1$  corresponds to  $\delta = 0$  and prolate/oblate superdeformed shapes  $\eta = 2^{\pm 1}$  corresponds to  $\delta = \pm \log 2 \approx \pm 0.69$ . The system with spheroidal power-law potential is non-integrable except for two limits  $\alpha = 2$  (HO) and  $\alpha = \infty$  (cavity). In Fig. 8, we show Poincaré surface of section for  $\alpha = 2, 5, 20$  and  $\infty$ , each with  $\eta = \sqrt{3}$  ( $\delta \approx 0.49$ ). It is found that some complex structures emerge in the Poincaré plots with increasing  $\alpha > 2$ , and the surface becomes most chaotic around  $\alpha \sim 20$ , then it turns into simpler structure for extremely large  $\alpha$ .

Figure 9 shows the single-particle spectra as functions of spheroidal deformation parameter  $\delta$ . The value of radial parameter is put  $\alpha = 5.0$ , corresponding to medium-mass nuclei. The degeneracies of levels at spherical shape are resolved and shell structure changes as varying deformation. The level diagram is similar to what obtained for MO or WS/BP models without spin-orbit coupling. One of its characteristic features in comparison to HO model is the asymmetry of deformed shell structures in prolate and oblate sides. This asymmetry becomes more pronounced for larger  $\alpha$ , and it might be regarded as the origin of prolate-shape dominance in nuclear ground-state deformations. We shall discuss the semiclassical origin of the above asymmetry in the following subsections.

In order to see the dependence on shape parametrization, we also calculated the deformed quantum spectra for

quadrupole deformation, which might be more popular in earlier studies,

$$f(\theta) = \frac{1 + \beta_2 P_2(\cos \theta)}{\sqrt[3]{1 + \frac{3}{5}\beta_2^2 + \frac{2}{35}\beta_2^3}}. \quad (4.3)$$

The factor in the denominator arranges the conservation of volume surrounded by equi-potential surface. Figure 10 show Poincaré surface of section for quadrupole deformations  $\beta_2 = 0.3$  and  $0.4$  with  $\alpha = 5.0$ . Comparing with right upper panel in Fig. 8, one will see that the particle motions in quadrupole potential are more chaotic than those in spheroidal potential.

Figure 11 shows the level diagram for quadrupole deformation. Although the properties of classical motions are quite different from those in spheroidal potential, the deformed shell structures are very similar to each other. Thus, the above difference of shape parametrization does not cause a serious difference in the gross shell structures at normal deformations. Notable effects of chaoticity in quadrupole potential can only be seen in the strong level repulsions at large deformations  $\beta_2 \gtrsim 0.3$ . Therefore, we shall only consider the spheroidal deformation in the following analysis.

### B. Prolate-oblate asymmetry in deformed shell structures

Let us examine the properties of deformed shell structures in normal deformation region ( $|\delta| \lesssim 0.3$ ). As shown in Figs. 9 and 11, single-particle spectra in a potential with sharp surface show prolate-oblate asymmetry (in the sense discussed in Sec. I). Hamamoto and Mottelson[7] paid attention on the different ways of level *fanning* (from the terminology used in [7]) in oblate and prolate sides; level fanning is considerably suppressed in the oblate side as compared to the prolate side. Due to that suppression of level fanning, shell structures in the oblate shapes are similar to that of spherical shape and system has smaller chance to gain shell energy by means of oblate deformation. This may explain the feature of prolate-shape dominance. They have shown that the above asymmetric way of level fanning can be understood from the interaction between single-particle levels which acts to suppress the level repulsions in oblate side for a potential with sharp surface. It clearly explains the fact that the asymmetry becomes more pronounced for heavier nuclei e.g., in Woods-Saxon model[9].

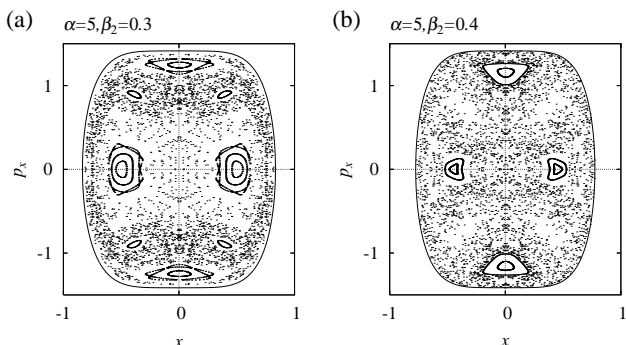


FIG. 10. Same as Fig. 8 but for quadrupole deformations  $\beta_2 = 0.3$  and  $0.4$  with  $\alpha = 5.0$ .

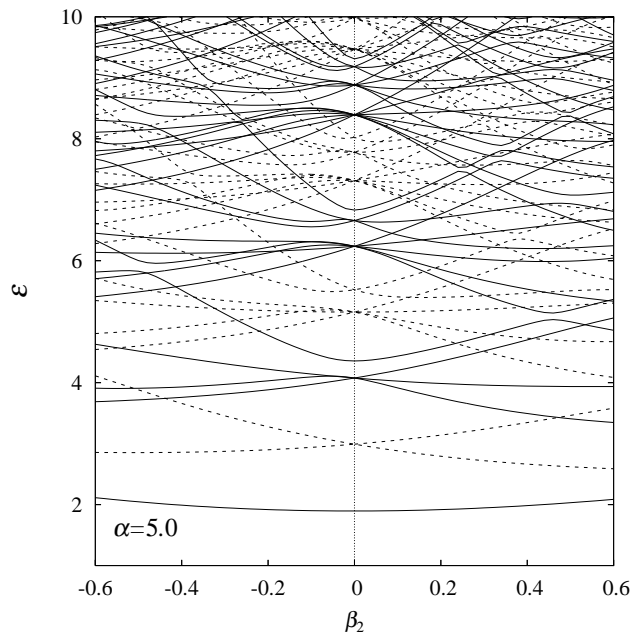


FIG. 11. Same as Fig. 9 but as functions of quadrupole deformation parameter  $\beta_2$ .

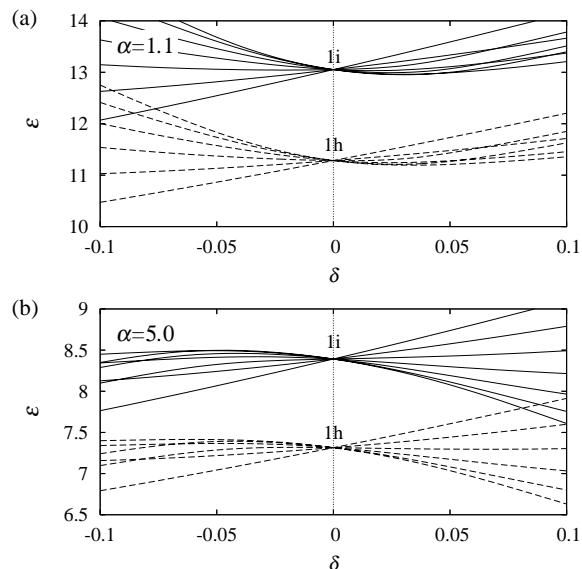


FIG. 12. Fanning of single-particle levels 1h (dashed lines) and 1i (solid lines) for  $\alpha = 5.0$  (lower panel) and  $\alpha = 1.1$  (upper panel).

The same kind of asymmetry is also found in the spectrum of Nilsson model.

In spheroidal power-law potential model, the asymmetry in level fanning becomes more pronounced for larger  $\alpha$  as expected. In the lower panel of Fig. 12, fannings of some  $nl$  levels ( $n$  and  $l$  represent principal and azimuthal quantum numbers, respectively) are illustrated for  $\alpha = 5.0$ . One sees that the level fannings are considerably suppressed in oblate side as in cavity potential.

It is interesting to note that if we take the radial parameter

$\alpha < 2$  (although it does not correspond to actual nuclear situations), the way of level fanning becomes just opposite to the case of  $\alpha > 2$ . As one see in the upper panel of Fig. 12), level spreading is suppressed in the prolate side. We will discuss later if it causes oblate-shape dominance.

Following the analysis in Ref. [7], we calculate the deformation energy

$$E_{\text{def}}(A, \delta) = E(A, \delta) - E(A, 0) \quad (4.4)$$

and compare the energies in prolate and oblate sides at each local minima. Here, we assume the same single-particle spectra for neutrons and protons and only consider  $N = Z$  even-even nuclei for simplicity. The sum of single-particle energies for nucleus of mass number  $A$  is given by

$$E_{sp}(A) = 4 \sum_{i=1}^n e_i, \quad A = N + Z = 4n. \quad (4.5)$$

Using the Strutinsky method, the above energy can be decomposed into smooth part  $\tilde{E}_{sp}(A)$  and oscillating part  $\delta E(A)$ . As in usual, we can expect that the above oscillating part represents the correct quantum shell effect of many-body system. In Strutinsky's shell correction method, the smooth part is replaced with the phenomenological liquid drop model (LDM) energy to get the total many-body energy, but here we try to extract the smooth part also from the single-particle energies. In mean-field approximation, single particle Hamiltonian is written as

$$\hat{h} = \hat{t} + \hat{\Gamma} \quad (4.6)$$

where  $\hat{t}$  and  $\hat{\Gamma}$  represent kinetic energy and mean-field potential, respectively, and  $\hat{\Gamma}$  is currently given by the power-law potential. In this case, by the use of Virial theorem, average of  $\hat{t}$  and  $\hat{\Gamma}$  are in ratio  $2\langle \hat{t} \rangle = \alpha \langle \hat{\Gamma} \rangle$ , and one obtains

$$\langle \hat{t} \rangle = \frac{\alpha}{\alpha + 2} \langle \hat{h} \rangle, \quad \langle \hat{\Gamma} \rangle = \frac{2}{\alpha + 2} \langle \hat{h} \rangle. \quad (4.7)$$

Therefore, the smooth (average) part of the  $A$ -body energy is given approximately by

$$\tilde{E}(A) \approx \left\langle \sum_i \hat{t}_i + \frac{1}{2} \sum_i \hat{\Gamma}_i \right\rangle = \frac{\alpha + 1}{\alpha + 2} \tilde{E}_{sp}(A) \quad (4.8)$$

This expression will be valid for many-body systems interacting with 2-body interaction. Thus, we calculate the  $A$ -body energy by

$$E(A) = \frac{\alpha + 1}{\alpha + 2} \tilde{E}_{sp}(A) + \delta E(A) \quad (4.9)$$

Figure 13 compares the local minima of deformation energies (4.4) in prolate and oblate sides. At the HO value ( $\alpha = 2.0$ ), prolate and oblate deformed shell structures are symmetric and the deformation energies are comparable with each other. For  $\alpha > 2$  (two bottom panels), the deformation energies in prolate side become considerably lower than in oblate side as the radial parameter  $\alpha$  becomes larger. The power-law potential model thus reproduce correctly the feature of prolate-shape dominance in nuclear deformation.

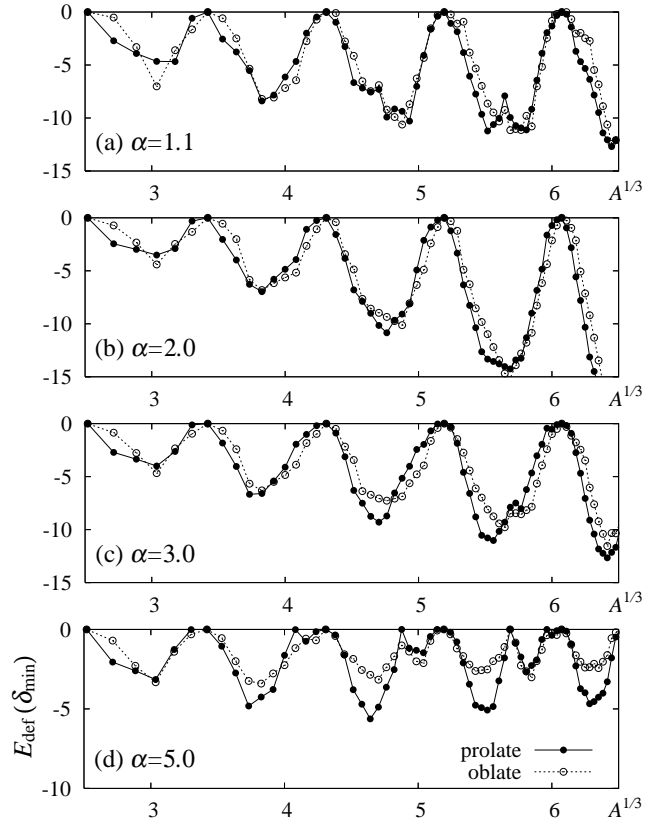


FIG. 13. Deformation energies (4.4) of prolate and oblate states at each local minima. Deformation energy  $E_A(\delta)$  is calculated as function of deformation  $\delta$  and its minimum values for prolate and oblate sides are plotted with filled and open circles, respectively.

For  $\alpha < 2$ , as shown in the top panel of Fig. 13, we find no indication of oblate-shape dominance in spite of the feature of level fanning shown in the upper panel of Fig. 12. Some nuclei have lowest energies at oblate shapes  $\delta \sim -0.3$ , but the difference in energies between prolate and oblate minima are generally small. Therefore, one cannot fully explain the prolate(oblate)-shape dominance only by the ways of level fanning.

In order to analyze shape stability, we define *shell-deformation energy* using the smooth part of energy at spherical shape as reference,

$$\Delta E(A, \delta) = E(A, \delta) - \tilde{E}(A, 0) \quad (4.10)$$

with (4.8) and (4.9). (Note that the 2nd term of (4.10) is not  $\tilde{E}(A, \delta)$ , so that  $\Delta E$  contains smooth part of deformation energy.) Figure 14 shows contour plots of  $\Delta E$  for  $\alpha = 1.1$  and 5.0 as functions of deformation  $\delta$  and mass number  $A$ . They show some deep minima on  $\delta = 0$  line at values of  $A$  corresponding to spherical magic numbers. The valley lines run through these minima and the deformation energy minima distribute along these valleys. For  $\alpha = 5.0$ , the valley lines have large slopes in the prolate side and deep energy minima are formed at  $\delta \sim 0.2$  between spherical magics, while the valley lines are almost flat in the oblate side. This is essentially the same behavior as what Frisk found for the spheroidal

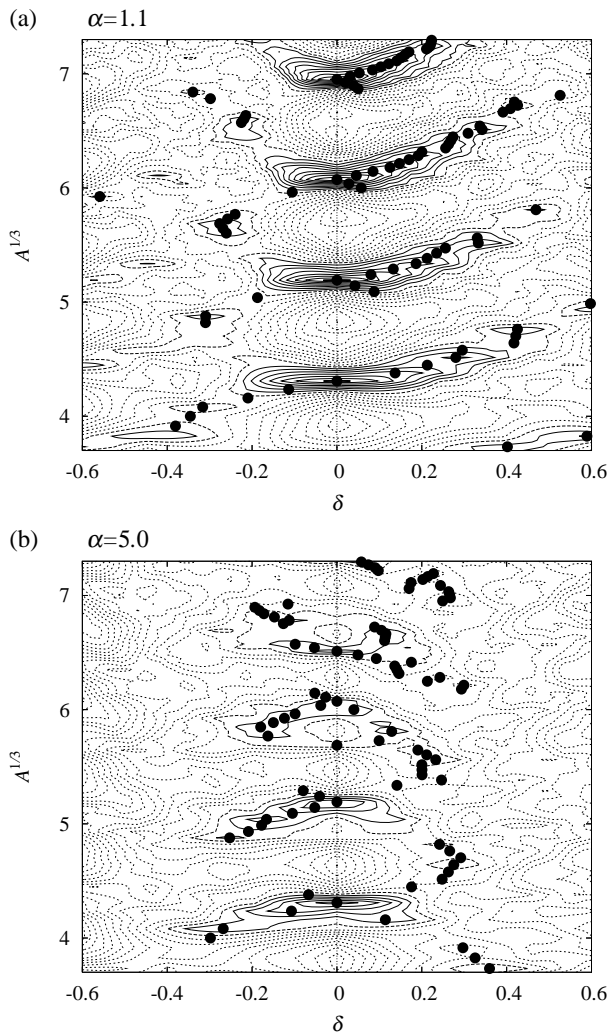


FIG. 14. Contour plot of the A-body shell-deformation energy (4.10) in deformation-mass number plane ( $\delta, A^{1/3}$ ) for  $\alpha = 1.1$  (upper panel) and  $\alpha = 5.0$  (lower panel). Solid and dashed contour lines represent negative and positive values, respectively. Dots represent values of deformation parameter at absolute energy minima for each A.

cavity[10]. For  $\alpha = 1.1$ , the valley lines have larger slope in the oblate side, but the slope in prolate side is not as small as in oblate side for  $\alpha = 5.0$  and the deformation energy minima distribute mainly along the valley lines in the prolate side. One can find rather deep energy minima at  $\delta \sim -0.3$  for particle numbers between spherical magics, but the energy difference between oblate and prolate local minima are generally small. Thus, for an understanding of prolate-shape dominance, it is critical to explain the asymmetric behavior of the slopes of the energy valleys.

Since shell energy takes deep negative value when the single-particle level density at the Fermi energy is low, let us investigate the coarse-grained single-particle level density as functions of energy and deformation. Figure 15 shows the oscillating part of coarse-grained single-particle level density for  $\alpha = 1.1$  and 5.0 plotted as functions of deformation  $\delta$  and scaled energy  $\mathcal{E}$ . They show regular ridge-valley struc-

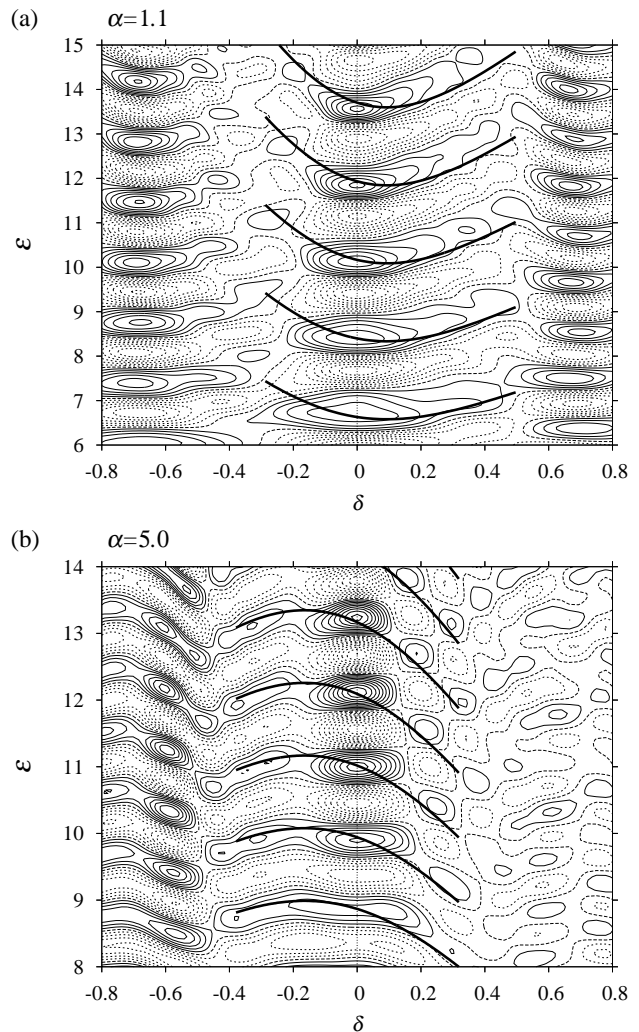


FIG. 15. Contour plot of oscillating level density for radial parameter  $\alpha = 1.1$  (upper panel) and 5.0 (lower panel) in deformation-energy plane ( $\delta, \mathcal{E}$ ). For calculation of coarse-grained level density, smoothing width  $\Delta\mathcal{E} = 3.0$  is taken. Solid and dashed contour lines represent negative and positive values, respectively. Thick solid lines represent constant-action lines (4.13) for the bridge orbits M(1,1).

tures similar to shell energy. Therefore, for an understanding of prolate-shape dominance, it is essential to investigate the origin of the above ridge-valley structures in deformed single-particle level density. For the spheroidal cavity potential, Frisk ascribed it to the change of the action integrals along the triangular and rhomboidal orbits in the meridian plane, for which the volume conservation condition plays an important role[10]. We are going to study the case of more realistic power-law potential.

In the following subsections, we will show that the above ridge-valley structure can be explained in connection with classical periodic orbits using semiclassical periodic-orbit theory. The thick solid curves in Fig. 15 represent the semiclassical prediction of the valley lines which will be discussed in Sect. IV D.

### C. Periodic orbits in spheroidal potential

In order to examine the semiclassical origin of the above asymmetry in deformed shell structure using periodic orbit theory, we first consider the properties of classical periodic orbits in spheroidal power-law potential and their bifurcations. For spherical potential, all the periodic orbits are planar and degenerate with respect to rotations. The degree of degeneracy for the orbit family is described by degeneracy parameter  $\mathcal{K}$  which represents the number of independent continuous parameters required to specify a certain orbit in the family. The maximum value of  $\mathcal{K}$  is equal to the number of independent symmetric transformations of the system. The isolated orbits have  $\mathcal{K} = 0$ . In spherical cavity potential, degeneracy parameter is  $\mathcal{K} = 3$  for generic periodic orbits, and  $\mathcal{K} = 2$  for diametric and circular orbits which are transformed onto themselves by one of the rotations. If the spheroidal deformation is added to the potential, generic planar orbits bifurcate into two branches: One is the orbit in equatorial plane and the other is the orbit in meridian plane (plane containing symmetry axis). All but two exceptional orbits degenerate with respect to the rotation about symmetry axis, and the degeneracy parameter is  $\mathcal{K} = 1$ . The diametric orbit bifurcate into degenerate family of equatorial diametric orbits ( $\mathcal{K} = 1$ ) and isolated diametric orbit along symmetry-axis ( $\mathcal{K} = 0$ ). The circular orbit bifurcate into isolated equatorial circular orbit ( $\mathcal{K} = 0$ ) and oval-shape orbit in meridian plane ( $\mathcal{K} = 1$ ). With increasing deformation towards prolate side ( $\delta > 0$ ), the equatorial orbits undergo successive *period-multiplying bifurcations* and new 3D orbits emerge. In the oblate side, diametric orbit along the symmetry-axis undergoes successive period-multiplying bifurcations and generate new meridian-plane orbits. These new-born 3D and meridian-plane orbits have hyperbolic caustics and are sometimes called *hyperbolic orbits*.

It is very interesting to note that the above new-born hyperbolic orbits from equatorial orbits are distorted towards symmetry axis as increasing deformation and finally submerge into diametric orbit along symmetry-axis. (Some 3D orbits submerge into other hyperbolic orbits before submerging into symmetry-axis orbit at last.) In this way, the hyperbolic orbits make bridges between the equatorial and symmetry-axis orbits, and we shall call those hyperbolic orbits as “bridge orbits”[33, 34]. As increasing  $\delta$ , periods of equatorial orbit decrease while that of symmetry-axis orbit increases. At each crossing point of the periods (or actions) of repeated equatorial and symmetry-axis orbits, bridge orbit exist to intervene them.

Accordingly, we shall classify periodic orbits in spheroidal power-law potential into the following 4 groups:

- i) *Isolated orbits* ( $\mathcal{K} = 0$ ): This group consists of the diametric orbit along symmetry axis ( $z$ -axis), denoted “Z”, and the circular orbit in equatorial plane, denoted “EC”. Orbit EC is stable both in the prolate and oblate sides, whose repeated period-multiplying bifurcations generate 3D bridge orbits. Orbit Z is stable in the oblate side and undergoes successive period-multiplying bifurcations, while its stability alternate in the prolate side with repeated bifurcations which absorb bridge orbits.
- ii) *Equatorial-plane orbits* ( $\mathcal{K} = 1$ ): This corresponds to

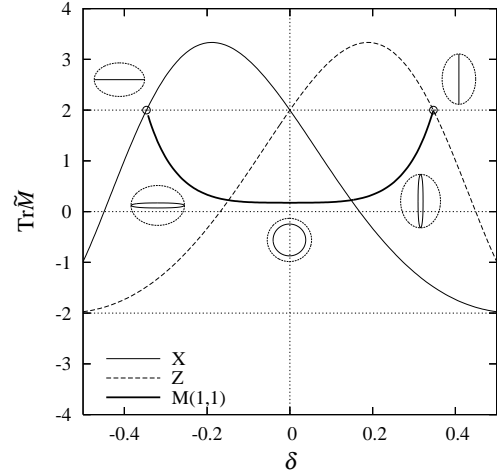


FIG. 16. Bifurcation diagram for  $M(1,1)$  bridge orbit between  $X$  and  $Z$  orbits for  $\alpha = 3.0$ . Traces of symmetry-reduced monodromy matrix  $\bar{\mathbf{M}}$  are plotted as functions of deformation parameter  $\delta$ . Bifurcation points ( $\text{Tr}\bar{\mathbf{M}} = 2$ ) are indicated by open circles. Shapes of the periodic orbits as well as equi-potential surface are also shown.

the equatorial-plane branch of the deformation-induced bifurcation. They have the same shapes as those in spherical potential shown in Fig. 5. They are denoted  $E(k, m)$ , where  $k$  is the number of vertices (corners) and  $m$  is the number of rotation. Diametric orbit is especially denoted “X” (which include the orbits along  $x$  axis).

- iii) *Meridian-plane orbits* ( $\mathcal{K} = 1$ ): This corresponds to the meridian-plane branch of the deformation-induced bifurcation. They survive up to any large deformation, keeping their original geometries.
- iv) *Bridge orbits* ( $\mathcal{K} = 1$ ): These orbits emerge from the bifurcations of equatorial orbits. Meridian-plane orbits emerge from diametric orbits and submerge into repetitions of orbit  $Z$ . Non-planar 3D orbits emerge from non-diametric equatorial orbits, and they also submerge into the orbit  $Z$ . Some of them submerge into other bridge orbit before submerging into  $Z$ . The meridian-plane bridge intervening  $mX$  ( $m$ -th repetition of  $X$ ) and  $nZ$  ( $n$ -th repetition of  $Z$ ) is denoted  $M(m, n)$ . Except for  $M(1,1)$  bridge, a pair of stable and unstable bridge orbits emerge, and are denoted  $M(m, n)_s$  and  $M(m, n)_u$ , respectively. 3D bridge  $B(m, m, n)$  emerge via *pitchfork bifurcation* of equatorial  $mEC$  ( $m$ -th repetitions of  $EC$ ), and submerge into  $M(m, n)$  orbit before finally submerge into  $nZ$ . The other 3D bridges intervening equatorial  $E(k, m)$  and  $nZ$  emerges as a stable and unstable pair, and denoted as  $B(k, m, n)_{s,u}$ . As increasing deformation, they first submerge into 3D bridge  $B(m, m, n)$ , which will submerge into  $M(m, n)$  and finally into  $nZ$ .

Figure 16 shows bifurcation diagram for bridge orbit  $M(1,1)$  for  $\alpha = 3.0$ . The traces of  $(2 \times 2)$  symmetry-reduced monodromy matrices for relevant periodic orbits are plotted as functions of deformation parameter  $\delta$ . The  $\mathcal{K} = 1$  family

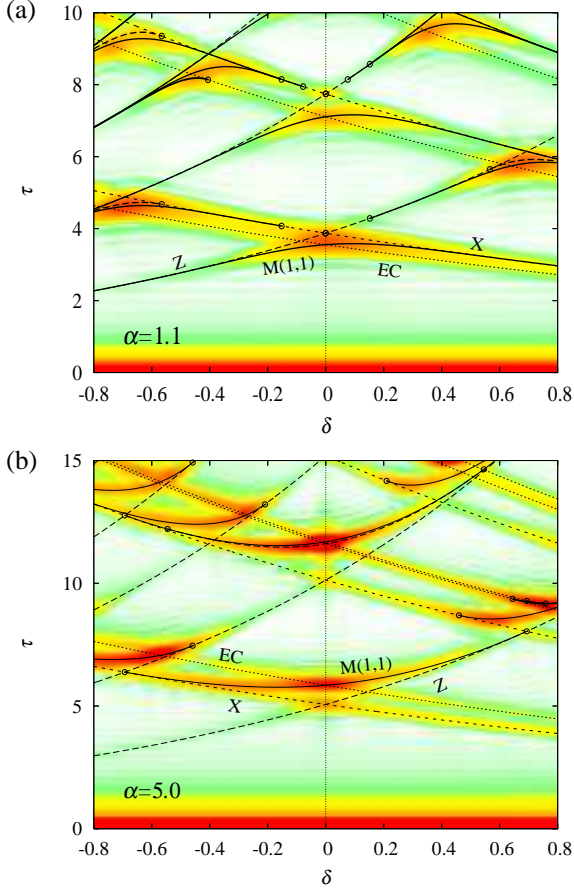


FIG. 17. (color online) Modulus of Fourier transform of the level density is shown by gray-scale plot as a function of deformation parameter  $\delta$  and scaled period  $\tau$ . Scaled periods of classical periodic orbits are also displayed.

of equatorial diameter orbit X undergoes pitchfork bifurcation at  $\delta = -0.34$  and a family of oval-shape meridian-plane orbit M(1,1) emerge. In the limit  $\delta \rightarrow 0$ , the shape of M(1,1) orbit approaches circle, and it associates with equatorial circular orbit EC to form  $\mathcal{K} = 2$  family. At  $\delta > 0$  it bifurcates into equatorial EC and meridian M(1,1) family again. The meridian branch submerge into the orbit Z at  $\delta = 0.34$  via pitchfork bifurcation. Thus, the orbits M(1,1) make bridge between two diametric orbits X and Z.

In the HO limit,  $\alpha \rightarrow 2$ , the bridge shrinks to a crossing point of X and Z orbits and can exist only at  $\delta = 0$  (spherical shape), where they altogether form a degenerate  $\mathcal{K} = 2$  family. With increasing  $\alpha$ , the bridge orbit exist in wider range of deformation over the crossing point. In the cavity limit,  $\alpha \rightarrow \infty$ , this orbit approaches so-called *creeping orbit* or *whispering gallery orbit*, which runs along the boundary.

#### D. Semiclassical origin of prolate-oblate asymmetry

To see the effect of the above bifurcation to the shell structure, we calculate Fourier transform of level density (2.30) with the obtained quantum spectra. In Fig. 17, modulus of

Fourier transform  $|F(\tau, \delta)|$  is shown in gray-scale plot as a function of deformation  $\delta$  and scaled period  $\tau$ . Scaled periods of classical periodic orbits  $\tau_\beta(\delta)$  are also drawn by lines. One sees nice correspondence between quantum Fourier amplitude and classical periodic orbits. Particularly, one can find significant peaks along the bridge orbit M(1,1), which indicate that the shell structure in normal deformation region is mainly determined by the contribution of this bridge orbit.

Let us assume that a contribution of single orbit (or degenerate family)  $\beta$  dominate the periodic orbit sum, namely,

$$\delta g(\mathcal{E}) \approx A_\beta \cos(\mathcal{E} \tau_\beta - \frac{\pi}{2} \nu_\beta). \quad (4.11)$$

Then, the valley lines of level density should run along the curves where above cosine function takes the minimum value  $-1$ , namely,

$$\mathcal{E} \tau_\beta - \frac{\pi}{2} \nu_\beta = (2n + 1)\pi, \quad n = 0, 1, 2, \dots \quad (4.12)$$

In Fig. 15, we plot this constant-action curves

$$\mathcal{E} = \frac{(2n + 1 + \frac{1}{2} \nu_\beta) \pi}{\tau_\beta(\delta)} \quad (4.13)$$

for bridge orbit M(1,1). We see that the constant-action lines of the bridge orbit nicely explain the ridge-valley structure in quantum level density. Properties of deformed shell energy minima in Fig. 14 are thus understood as the effect of bridge orbit contribution. For  $\alpha > 2$ , bridge orbits appear upward from the crossing point of two diametric orbits X and Z in  $(\delta, \tau)$  plane. Note that the scaled action of orbit Z has larger slope than that of orbit X in  $(\delta, \tau)$  plane. This difference comes from the fact that the lengths of semiaxes  $R_z$  and  $R_\perp$  in a volume-conserved spheroidal body are proportional to the different powers of deformation parameter  $\delta$  as in Eq. (4.2). The scaled period of the diametric orbit along  $i$ -th axis is proportional to the length of corresponding semiaxis  $R_i$ ;

$$\tau_i = \tau_0^D \frac{R_i}{R_0},$$

where  $\tau_0^D$  is the scaled period of the diametric orbit at spherical shape. Using Eq. (4.2), one has

$$\tau_X = \tau_0^D e^{-\frac{1}{3}\delta}, \quad \tau_Z = \tau_0^D e^{\frac{2}{3}\delta}. \quad (4.14)$$

Therefore, the bridge between X and Z orbits have large slope in prolate side while it is almost flat in oblate side. This clearly explains the profile of ridge-valley structures in level density and shell energy. With increasing  $\alpha$ , triangular- and square-type orbits emerge at  $\alpha = 7$  and 14, respectively, via the *isochronous* bifurcations of circular orbit (see Eq. (3.7) for  $m = 1$ ) for spherical shape. With spheroidal deformation, they bifurcate into equatorial and meridian branches, which are both singly degenerated due to the axial symmetry. For finite  $\alpha$ , they submerge into oval orbit and finally into diametric orbit at large deformation. In this sense, they are also bridge orbits intervening two diametric orbits. These meridian orbits survive up to larger deformation as increasing  $\alpha$ , and in the cavity limit ( $\alpha \rightarrow \infty$ ), they survive for any large deformation. Therefore, the meridian orbits in cavity potential can be regarded as a limit of bridge orbits. Thus we see that the Frisk's

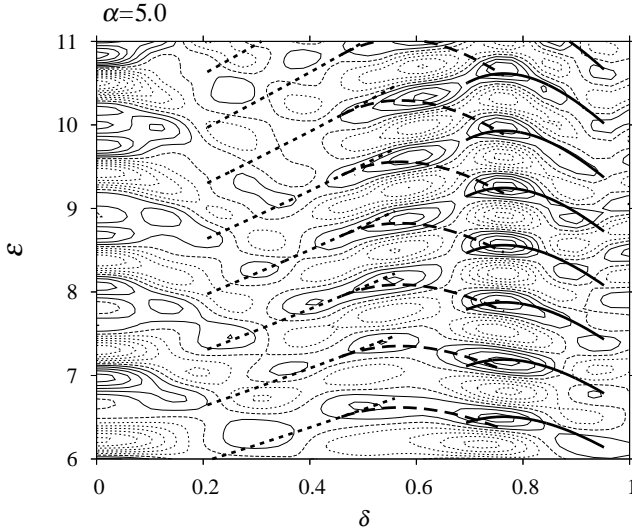


FIG. 18. Contour plot of oscillating level density for radial parameter  $\alpha = 5.0$  around prolate superdeformed region. Smoothing width  $\Delta\mathcal{E} = 0.2$  is taken. Solid and dashed contour lines represent negative and positive values, respectively. Thick dotted, dashed and solid lines represent constant action lines (4.13) of periodic orbits 2X, M(2,1) and B(2,2,1), respectively.

argument for spheroidal cavity system[10] is continuously extended to the case of finite diffuseness.

For  $\alpha < 2$ , bridge orbit appear in opposite side of the crossing point and its slope becomes larger in oblate side. This also explains the profile of valley lines in level density and shell energy for  $\alpha = 1.1$  in Figs. 15 and 14.

### E. Superdeformed shell structures

In axially deformed harmonic oscillator (HO) potential model, one sees simultaneous degeneracy of many energy levels at rational axis ratios. HO is often used for the nuclear mean-field potential in the limit of light nuclei. In HO model, superdeformation is explained as the result of strong level bunching at axis ratio 2:1. Search of much larger deformation originated from the strong level bunching at axis ratio 3:1 (sometimes referred to as *hyperdeformation*) has also been a challenging experimental and theoretical problem. On the other hand, spheroidal cavity model, which is used as the limit of potential for heavy nuclei, also show superdeformed shell structure while it is much weaker than that found in oscillator model. In the spheroidal cavity model, superdeformed shell structures are intimately related with emergence of meridian and 3D orbits which oscillate twice in the short axis direction while it oscillates once in the long axis direction, just as the degenerate 3D orbits in 2:1 axially-deformed HO potential[11]. One may expect to have a *unified* semiclassical understandings for the origin of superdeformed shell structures found in the above two limiting cases by connecting them with power-law potential model.

Figure 18 shows the oscillating part of the coarse-grained level density for radial parameter  $\alpha = 5.0$  and deformation  $\delta$  around superdeformed region. It clearly show that new regu-

larities in shell structure are formed at superdeformed region. The valley lines are up-going till  $\delta \sim 0.5$ , and they bent down around  $\delta \sim 0.6$ . One sees another deep minima at  $\delta \gtrsim 0.7$ . Let us examine their semiclassical origins.

For  $\alpha > 2$ , one finds bridge orbits M(2,1) which intervenes orbits 2X (2nd repetitions of X) and Z. Figure 19 is the bifurcation diagram for the orbits relevant to this bifurcation, calculated for  $\alpha = 3.0$ . The orbit X undergoes period doubling bifurcation at  $\delta = 0.55$  and emerge a pair of bridge orbits M(2,1)<sub>s</sub> (stable) and M(2,1)<sub>u</sub> (unstable). They have shapes of boomerang and butterfly as shown in Fig. 19. As increasing  $\delta$ , those orbits are distorted towards  $z$  axis and finally submerge into the orbit Z at different values of  $\delta$  via pitchfork bifurcations.

For larger  $\alpha$ , various equatorial orbits appear as shown in Fig. 5, and they also undergo bifurcations by imposing deformation. Each of those bifurcation will generate a pair of 3D bridge orbits, which are also distorted towards symmetry axis by increasing  $\delta$  and finally submerge into Z. Figure 20 shows some 3D bridge orbits important for superdeformed shell structures for  $\alpha = 5.0$ . Equatorial circular orbit EC undergoes period-doubling bifurcation which is peculiar to 3D system and generate 3D bridge orbit B(2,2,1). Equatorial orbit E(5,2) undergoes non-generic period doubling bifurcation and a pair of 3D bride orbits (5,2,1)<sub>s,u</sub> emerge. All the above 3D orbits finally submerge into Z orbit by increasing deformation  $\delta$ . See Appendix A for detailed description of these 3D bridge orbit bifurcations.

Figure 21 shows Fourier transform of scaled-energy level density for  $\alpha = 5.0$  around superdeformed region. The scaled period of classical periodic orbits are also drawn with lines. The Fourier amplitude shows remarkable enhancement along the bridge orbits M(2,1) and B(5,2,1), indicating their significant roles in superdeformed shell structures.

The constant action lines (4.13) for M(2,1) and B(2,2,1) are shown in Fig. 18 with thick solid and broken lines. They perfectly explain the ridge-valley structures of quantum level densities. It shows the significant roles of bifurcations of M(2,1) and  $(n, 2, 1)$  orbits for enhanced shell effect at  $\delta \sim 0.5$  and 0.7, respectively.

M(2,1) and B(2,2,1) orbits shrink to the crossing point of 2X(2EC) and Z orbits in the HO limit,  $\alpha \rightarrow 2$ , and turns a  $\mathcal{K} = 4$  degenerate family. As increasing  $\alpha$ , the deformation range in which bridge orbit can exist becomes wider. Therefore, the bifurcation deformation of the orbits 2X and 2EC becomes smaller as increasing  $\alpha$  and the effect of these orbits take place at smaller deformation. This may explain the experimental fact that deformation of superdeformed band is smaller for heavier nuclei; e.g.,  $\beta_2 \sim 0.6$  for Dy region and  $\beta_2 = 0.4 \sim 0.5$  for Hg region[35, 36]. In the cavity limit  $\alpha \rightarrow \infty$ , the two meridian orbits M(2,1) and the two 3D orbits B( $n, 2, 1$ ) respectively join to  $\mathcal{K} = 1$  families, which survive for arbitrary large deformations.[11, 37]

In conclusion, the highly degenerate family of orbits in rational HO potential ( $\alpha = 2$ ) are *resolved* at  $\alpha > 2$  into two orbits, equatorial and symmetry-axis orbits who have less degeneracies, and the bridge orbit which mediate them within finite deformation range. The “length” of bridge in  $(\delta, \tau)$  plane grows as radial parameter  $\alpha$ , and the superdeformed shell structure is formed in smaller  $\delta$  for large  $\alpha$ , correspond-

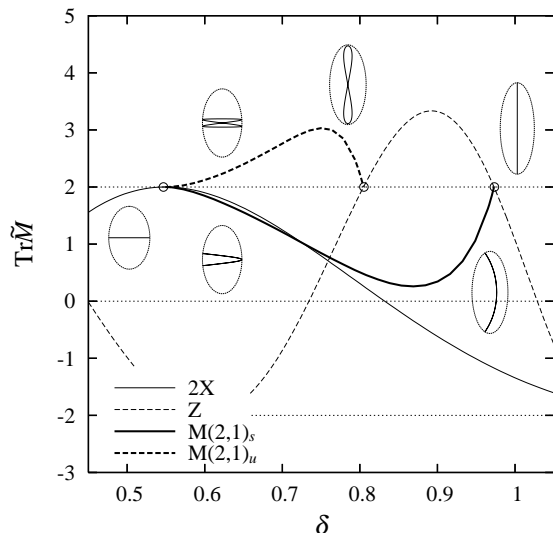


FIG. 19. Same as Fig. 16 but for  $M(2,1)$  bridge orbit between  $2X$  and  $Z$ , “ $2X$ ” represents 2nd repetition of  $X$ . The radial parameter  $\alpha = 3.0$  is used. A pair of bridge orbits emerge at  $\delta = 0.55$  via period-doubling bifurcation. The unstable branch  $M(2,1)_u$  and stable branch  $M(2,1)_s$  submerge into  $Z$  at  $\delta = 0.80$   $0.97$ , respectively, via pitchfork bifurcations.

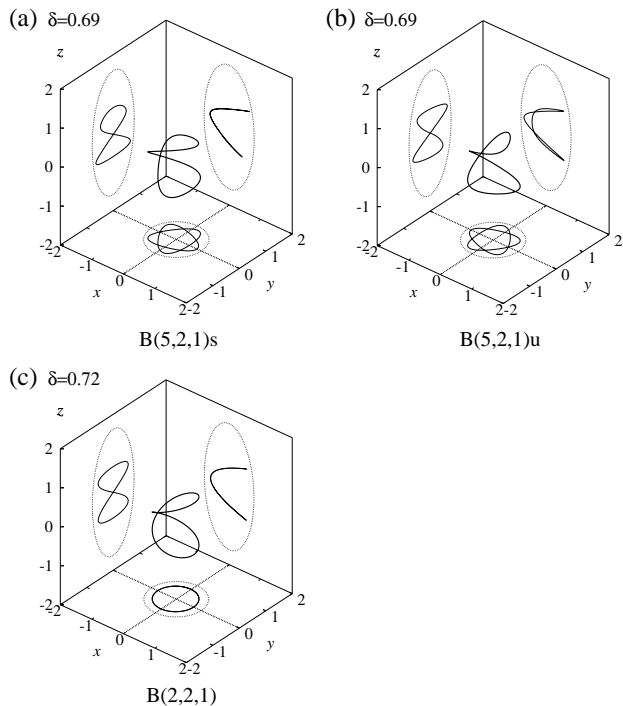


FIG. 20. 3D orbits responsible for superdeformed shell structure at  $\delta \sim 0.7$  and  $\alpha = 5$ . 3D plots and projections on  $(x,y)$ ,  $(x,z)$ ,  $(y,z)$  planes are shown as well as equi-potential surfaces.  $B(5,2,1)_s$  and  $B(5,2,1)_u$  are pair of stable and unstable 3D orbits emerge from equatorial orbit  $E(5,2)$ .  $B(2,2,1)$  emerge from 2nd repetition of equatorial circular orbit,  $2EC$ .

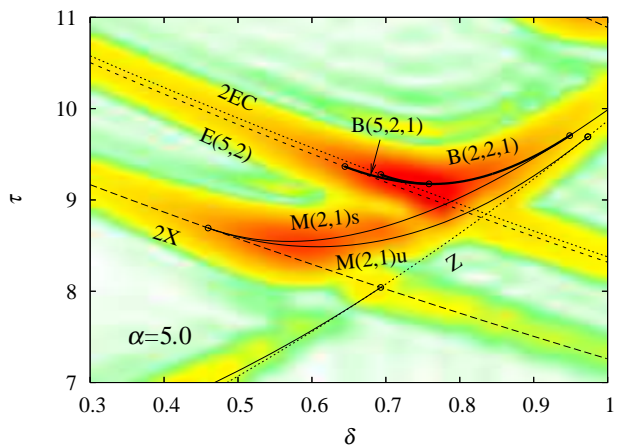


FIG. 21. (color online) Gray-scale plot of Fourier transform of the quantum level density (2.30) for radial parameter  $\alpha = 5.0$  as function of deformation  $\delta$  and scaled period  $\tau$ . The modulus of the Fourier transform has large value at dark region. The scaled periods of classical periodic orbits  $\tau_B$  are displayed with lines. Their bifurcation points are indicated by open circles.

ing to heavier nuclei, due to the strong shell effect brought about by the bridge-orbit bifurcation. In the  $\alpha \rightarrow \infty$  limit, some of the simplest bridge orbits coincide with meridian and 3D orbits emerging from the bifurcation of equatorial orbits at  $\delta = 0.5 \sim 0.6$  which play significant role in superdeformed shell structure in spheroidal cavity model[11, 12]. Thus, the semiclassical origin of superdeformed and hyperdeformed shell structures in HO and cavity models are unified as the two limiting cases of the contribution of bridge-orbit bifurcations.

## V. SUMMARY

We have made a semiclassical analysis of deformed shell structure with radial power-law potential model, which we introduce as realistic nuclear mean-field model (except for the lack of spin-orbit term in the current version) for stable nuclei in place of WS/BP models. We have shown that bridge orbits mediating equatorial and symmetry-axis orbits play significant role in normal and superdeformed shell structures. Particularly, prolate-oblate asymmetry of deformed shell structures, which is responsible for the prolate dominance in nuclear deformations, is clearly understood as the asymmetric slopes of bridge orbits in  $(\delta, \tau)$  plane. This asymmetry grows as increasing radial parameter  $\alpha$ , namely, as larger mass number  $A$ , which explain the fact that the prolate dominance is more remarkable in heavier nuclei. Some of these bridge orbits coincide with triangular and rhomboidal orbits in the cavity limit  $\alpha = \infty$ , whose significant contribution to the coarse-grained level density in spheroidal cavity and their roles in prolate-shape dominance was discussed by Frisk. Our results elucidate that the essence in semiclassical origin of prolate-shape dominance in cavity model also applies to more realistic power-law potential model. The semiclassical origin of superdeformed shell structures which have been discussed separately for oscillator and cavity models are continuously connected via bridge orbits in power-law potential models.

In this paper we have explored the contribution of periodic orbits via Fourier transform of quantum level density. In order to clarify the role of periodic-orbit bifurcation to the level density, it is important to establish semiclassical method with which we can evaluate contribution of classical periodic orbits in bifurcation region. Some preliminary results for spherical power-law potential using improved stationary phase method have been reported in [38]. Application of uniform approximation to this problem is also in progress.

Another important subject is the inclusion of spin degree of freedom. Since the nuclear mean field has strong spin-orbit coupling, it should be crucial to take account of its effect to analyze realistic nuclear shell structures. It is shown that the qualitative characters of deformed shell structures are not very sensitive to the spin-orbit coupling[9], however, it is reported that the prolate-shape dominance in nuclear ground-state deformation is realized after strong correlation with surface diffuseness and spin-orbit coupling. In Part. II, we will expand the model Hamiltonian to incorporate spin-orbit potential and discuss the nuclear problems which are closely related with spin degree of freedom due to the strong spin-orbit coupling. Some preliminary results have been reported in Ref. [15].

#### ACKNOWLEDGMENTS

The author thanks K. Matsuyanagi, M. Brack, A.G. Magner, Y.R. Shimizu and N. Tajima for discussions.

#### Appendix A: Bifurcations of 3D bridge orbits

For a periodic orbit in 2D autonomous Hamiltonian system, one can examine its bifurcation scenario by evaluating the trace of  $(2 \times 2)$  monodromy matrix as a function of control parameter such as deformation, strength of external field, or energy. 3D orbits in axially symmetric potential has  $(2 \times 2)$  symmetry-reduced monodromy matrix, but the ignored degree of freedom corresponding to symmetric rotation also play a role in bifurcation.

Figure 22 shows bifurcation diagram of periodic orbits responsible for superdeformed shell structures for  $\alpha = 5.0$ . The orbit X undergoes period-doubling bifurcation at  $\delta = 0.42$  and generate a pair of bridges  $M(2,1)_u$  and  $M(2,1)_s$ , which submerge into the orbit Z at  $\delta = 0.78$  and  $0.94$ , respectively. Equatorial circular orbit EC undergoes period-doubling bifurcation at  $\delta = 0.6$  and generate 3D bridge  $B(2,2,1)$ , which submerge into  $M(2,1)_s$  at  $\delta = 0.77$  before finally submerge into Z. Since EC is isolated, monodromy matrix has size  $(4 \times 4)$  and its four eigenvalues consists of two conjugate/reciprocal pairs. One of them are  $e^{\pm iv_c}$ , which represent stability against displacement in equatorial plane, whose values are independent of deformation  $\delta$  (2EC(1) in Fig. 22). The other pair  $e^{\pm iv_z}$ , which represent stability against displacement towards off-planar direction, change their values as function of deformation (2EC(2) in lower panel of Fig. 22). Bifurcation occurs when the latter eigenvalues become unity ( $v_z = 0$ ). The monodromy matrix of bridge  $B(2,2,1)$  has eigenvalues  $(e^{iv_c}, e^{-iv_c}, 1, 1)$  at its birth, and the first two eigenvalues change as increasing deformation. Therefore, the bifurcation

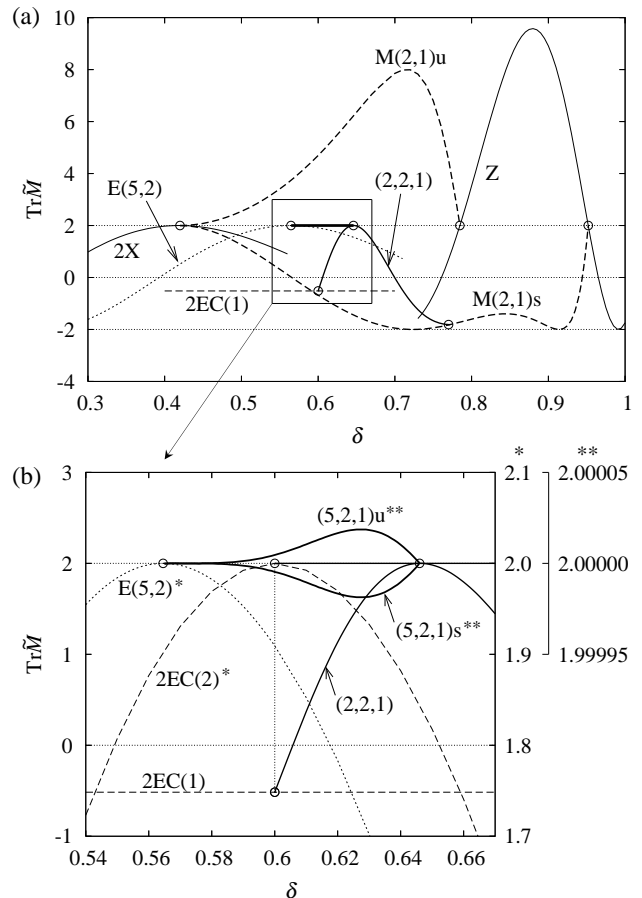


FIG. 22. Bifurcation diagram for periodic orbits around superdeformed region for  $\alpha = 5.0$ . Values of traces of the symmetry-reduced monodromy matrices are plotted as functions of deformation parameter  $\delta$ . The panel (b) is the magnified plot of the rectangular region indicated in the panel (a). For the orbit 2EC, traces of two  $(2 \times 2)$  sub-blocks in total  $(4 \times 4)$  monodromy matrix, denoted by 2EC(1) and 2EC(2), are plotted (see text). In the panel (b),  $\text{Tr}\tilde{\mathbf{M}}$  for orbits marked "\*" and "\*\*" are plotted in different scales indicated on the right vertical axis.

point does not correspond to  $\text{Tr}\tilde{\mathbf{M}} = 2$  for this bifurcation. The orbit  $B(2,2,1)$  submerge into  $M(2,1)$  at  $\delta = 0.77$ . This bifurcation point does not correspond to  $\text{Tr}\tilde{\mathbf{M}} = 2$ , either. Here, with decreasing  $\delta$ , the mother orbit  $M(2,1)_s$  pushes out a new orbit  $B(2,2,1)$  in direction of the eigenvector of  $\mathbf{M}$  belonging to one of the unit eigenvalues (other than which corresponding to the rotation about symmetry axis).

In general, real symplectic matrix  $\mathbf{M}$  can be transformed into Jordan canonical form by a suitable orthogonal transformation, and its  $(2 \times 2)$  sub-block associated with the unit eigenvalue generally has off-diagonal element  $v$ :

$$\mathbf{M} \sim \begin{pmatrix} 1 & v \\ 0 & 1 \end{pmatrix} \Big| \begin{matrix} \\ \\ \\ \tilde{\mathbf{M}} \end{matrix}$$

For finite  $v$ , there is only one eigenvector belonging to the unit eigenvalue, corresponding to the direction of symmetric rotation. This off-diagonal element varies as a function

of deformation, and vanishes at the bifurcation point, where  $\mathbf{M}$  acquires a new eigenvector perpendicular to the former one. Here, the symmetry-reduced monodromy matrix  $\tilde{\mathbf{M}}$  generally does not have unit eigenvalues. This is what occur in

the case of a 3D orbit bifurcations in axially symmetric potential, which is not detected from the trace of symmetry-reduced monodromy matrix.

- 
- [1] M. C. Gutzwiller, J. Math. Phys. **12**, 343 (1971).  
 [2] R. Balian and C. Bloch, Ann. Phys. **69**, 76 (1972).  
 [3] A. Bohr and B. R. Mottelson, *Nuclear Structure* (Benjamin, Reading, MA, 1975), Vol. II.  
 [4] N. Tajima, S. Takahara and N. Onishi, Nucl. Phys. A **603**, 23 (1996).  
 [5] N. Tajima and N. Suzuki, Phys. Rev. C **64**, 037301 (2001); N. Tajima, Y. R. Shimizu and N. Suzuki, Prog. Theor. Phys. Suppl. **146**, 628 (2002).  
 [6] S. Takahara, N. Onishi, Y. R. Shimizu and N. Tajima, Phys. Lett. B **702**, 429 (2011).  
 [7] I. Hamamoto and B. R. Mottelson, Phys. Rev. C **79**, 034317 (2009).  
 [8] H. Nishioka, K. Hansen and B. R. Mottelson, Phys. Rev. B **42**, 9377 (1990).  
 [9] V. M. Strutinsky, A. G. Magner, S. R. Ofengenden and T. Døssing, Z. Phys. A **283**, 269 (1977).  
 [10] H. Frisk, Nucl. Phys. A **511**, 309 (1990).  
 [11] K. Arita, A. Sugita and K. Matsuyanagi, Prog. Theor. Phys. **100**, 1223 (1998).  
 [12] A. G. Magner, K. Arita, S. N. Fedotkin and K. Matsuyanagi, Prog. Theor. Phys. **108**, 853 (2002).  
 [13] J. Carbonell, F. Brut, R. Arvieu and J. Touchard, J. of Phys. G **11**, 325 (1985).  
 [14] R. Arvieu, F. Brut, J. Carbonell and J. Touchard, Phys. Rev. A **35**, 2389 (1987).  
 [15] K. Arita, Int. J. Mod. Phys. E **13**, 191 (2004) (10th workshop on nuclear physics “Marie and Pierre Curie”, Proceedings, 2003, Kazimierz Dolny, Poland).  
 [16] S. Cwiok, J. Dudek, W. Nazarewicz, J. Skalski and T. Werner, Comp. Phys. Comm. **46**, 379 (1987).  
 [17] B. Buck and A. Pilt, Nucl. Phys. A **280**, 133 (1977).  
 [18] B. K. Jennings, Ann. Phys. (N.Y.) **84**, 1 (1974).  
 [19] M. Brack and R. K. Bhaduri, “*Semiclassical Physics*”, (Addison Wesley, 1997).  
 [20] M. Baranger, K. T. R. Davies and J. H. Mahoney, Ann. Phys. **186**, 95 (1988).  
 [21] A. M. Ozorio de Almeida and J. H. Hannay, J. Phys. A **20**, 5873 (1987).  
 [22] S. C. Creagh and R. G. Littlejohn, Phys. Rev. A **44**, 836 (1991).  
 [23] M. V. Berry and M. Tabor, Proc. R. Soc. Lond. A **349**, 101 (1976).  
 [24] M. Sieber, J. Phys. A **29**, 4715 (1996).  
 [25] H. Schomerus and M. Sieber, J. Phys. A **30**, 4537 (1997).  
 [26] M. Sieber and H. Schomerus, J. Phys. A **31**, 165 (1998).  
 [27] A. G. Magner, S. N. Fedotkin, K. Arita, T. Misu, K. Matsuyanagi, T. Schachner and M. Brack, Prog. Theor. Phys. **102**, 551 (1999).  
 [28] J. Kaidel and M. Brack, Phys. Rev. E **70**, 016206 (2004).  
 [29] K. Arita and M. Brack, Phys. Rev. E **77**, 056211 (2008).  
 [30] A. Sugita, K. Arita, and K. Matsuyanagi, Prog. Theor. Phys.  
 [31] V. M. Strutinsky, Nucl. Phys. A **95**, 420 (1967); *ibid.* **122**, 1 (1968).  
 [32] M. Brack and H. C. Pauli, Nucl. Phys. A **207**, 401 (1973).  
 [33] K. Arita and M. Brack, J. Phys. A **41**, 385207 (2008).  
 [34] Some bridge orbit bifurcations are exemplified in [33], and other ones are also found in:  
 M. Baranger and K. T. R. Davies, Ann. Phys. **177**, 330 (1987).  
 [35] P. J. Twin, Nucl. Phys. A **520**, 17c (1990).  
 [36] S. Åberg, Nucl. Phys. A **520**, 35c (1990).  
 [37] H. Nishioka, M. Ohta and S. Okai, Mem. Konan Univ. Sci. Ser. **38**(2), 1 (1991). (unpublished)  
 [38] A. G. Magner, I. S. Yatsyshyn, K. Arita, and M. Brack, Phys. Atom. Nucl. **74**, 1445 (2011).